Published in final edited form as:
Mol Cell. 2023 April 20; 83(8): 1237–1250.e15. doi:10.1016/j.molcel.2023.02.010.

Sequence and chromatin features guide DNA double-strand break resection initiation

Robert Gnügge[1,*], **Giordano Reginato**[2,3], **Petr Cejka**[2,3], **Lorraine S Symington**[1,4,5,*]

[1]Department of Microbiology & Immunology, Columbia University Irving Medical Center, New York, NY 10032, USA

[2]Department of Biology, Institute of Biochemistry, Eidgenössische Technische Hochschule (ETH), 8093 Zürich, Switzerland

[3]Institute for Research in Biomedicine, Università della Svizzera italiana (USI), Faculty of Biomedical Sciences, 6500 Bellinzona, Switzerland

[4]Department of Genetics & Development, Columbia University Irving Medical Center, New York, NY 10032, USA

[5]Lead contact

Summary

DNA double-strand breaks (DSBs) are cytotoxic genome lesions that must be accurately and efficiently repaired to ensure genome integrity. In yeast, the Mre11-Rad50-Xrs2 (MRX) complex nicks 5'-terminated DSB ends to initiate nucleolytic processing of DSBs for repair by homologous recombination. How MRX-DNA interactions support 5' strand-specific nicking and how nicking is influenced by the chromatin context have remained elusive. Using a deep sequencing-based assay, we mapped MRX nicks at single-nucleotide resolution next to multiple DSBs in the yeast genome. We observed that the DNA end-binding Ku70-Ku80 complex directed DSB-proximal nicks and that repetitive MRX cleavage extended the length of resection tracts. We identified a sequence motif and a DNA meltability profile that is preferentially nicked by MRX. Furthermore, we found that nucleosomes as well as transcription impeded MRX incisions. Our findings suggest that local DNA sequence and chromatin features shape the activity of this central DSB repair complex.

eTOC blurb

---

[*]Correspondence: robert.gnuegge@gmail.com (R.G.), lss5@cumc.columbia.edu (L.S.S.).

Author contributions
Conceptualization, R.G. and L.S.S.; Methodology, R.G. and L.S.S.; Software, R.G.; Formal Analysis, R.G. and G.R.; Investigation, R.G. and G.R.; Writing – Original Draft, R.G. and L.S.S.; Writing – Review & Editing, R.G., G.R, P.C. and L.S.S.; Visualization, R.G. and G.R.; Supervision, L.S.S. and P.C.; Funding Acquisition, L.S.S. and P.C.

Declaration of interests
The authors declare no competing interests.

The conserved Mre11-Rad50-Xrs2 (MRX) complex initiates homologous recombination by nicking DNA next to double-strand breaks (DSBs). Here, Gnuegge et al. show that the MRX nicking landscape next to DSBs is shaped by local nucleotide sequence and physical DNA features, as well as by end-binding proteins and the chromatin context.

Graphical Abstract

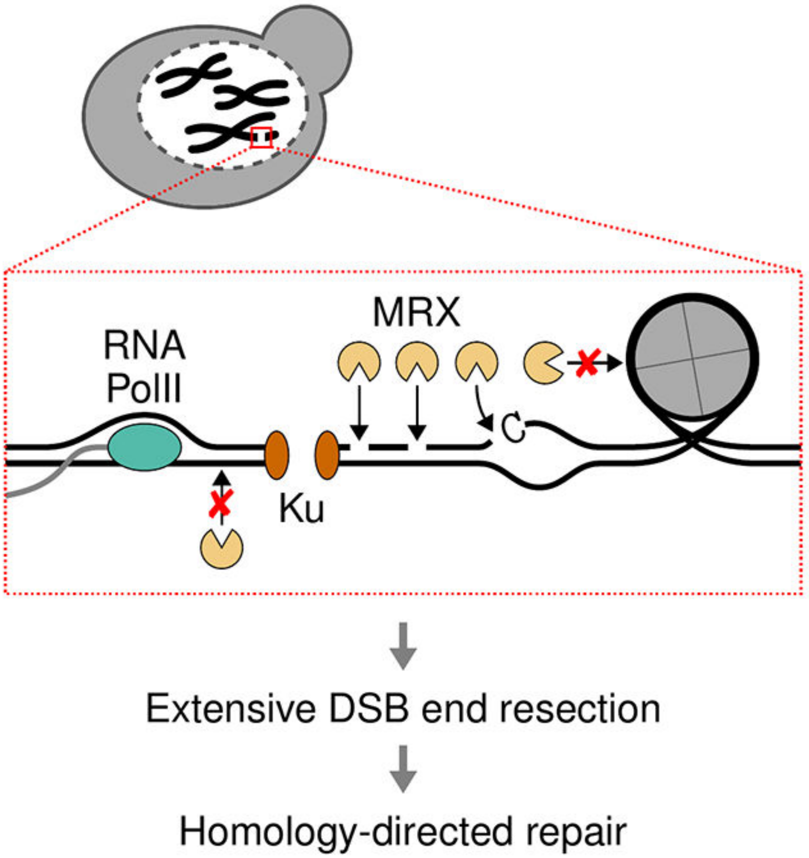

Keywords

DNA double-strand break; DNA repair; homologous recombination; resection; Mre11; Sae2; CtIP; chromatin

Introduction

DNA double strand breaks (DSB) are frequent genomic lesions that can be generated by exogenous sources, such as ionizing radiation, chemicals, or drugs, but can also result from endogenous metabolic processes [1]. Moreover, DSBs are intermediates of programmed cell developmental processes, including meiosis, and antibody and T cell receptor diversification [2]. DSBs must be efficiently and accurately repaired to ensure cell survival and genomic integrity. Consistently, DSB repair defects can result in chromosomal rearrangements and are associated with human diseases, such as immunodeficiency, neurological syndromes, premature aging, and cancer [3,4].

The two major pathways to repair DSBs are non-homologous end joining (NHEJ) and homologous recombination (HR). In NHEJ, the Ku70-Ku80 complex (Ku) binds to DSB ends to protect them from degradation and recruits additional NHEJ factors to re-ligate the ends [5]. HR starts with the nucleolytic degradation of DSB ends to generate 3'-terminated single-stranded DNA (ssDNA) overhangs in a process termed end resection [6]. The overhangs are coated by the ssDNA-binding RPA protein complex [7]. RPA is then replaced by the Rad51 recombinase, which mediates homology search and strand invasion into a repair template, forming a displacement loop (D-loop). The invading end is extended by DNA polymerases and is then channeled to the synthesis-dependent strand annealing (SDSA) pathway or double-Holliday junction resolution to ultimately heal the DSB.

The initiation of end resection is a critical determinant of repair pathway selection, as ssDNA overhangs are poor substrates for Ku binding and, thus, suppress NHEJ and favor HR [8]. Furthermore, efficient and symmetric resection at both ends of a DSB determines repair outcomes [9]. End resection is considered a two-step process consisting of short-range and subsequent long-range resection. In the first step, the Mre11-Rad50-Xrs2/NBS1 (MRX in *Saccharomyces cerevisiae*, MRN in mammals) complex initiates end resection by nicking the 5' strands internal to the DSB ends [10]. Mre11 endonuclease activity depends on its cofactor Sae2 (CtIP) and the latter's phosphorylation by cyclin-dependent kinase, therefore, restricting end resection to cell cycle phases where the sister chromatid is available as a repair template [10–12]. Moreover, various protein blocks, such as the Ku complex, have been shown to stimulate MRX/N nicking *in vitro* [10,13–15]. The nick serves as the entry point for bidirectional resection, whereby the Mre11 3'-5' exonuclease activity resects DNA back towards the break, while the redundant long-range resection factors Exo1 and Sgs1-Dna2 (BLM/WRN-DNA2) resect in the 5'-3' direction [6,16–19].

In vitro studies suggest an MRX nicking mechanism, where the complex binds DNA in the vicinity of a DSB [20]. MRX next undergoes extensive ATP hydrolysis-driven conformational changes, which might deform the bound DNA and lead to local DNA melting or bending [21–25]. The 5' DNA strand can then access the Mre11 nuclease site for nicking [26]. However, if this mechanism applies to MRX nicking *In vivo* and how the local sequence and chromatin contexts influence MRX cleavage is unclear.

Here we monitored MRX nicking at single-nucleotide (nt) resolution *in vivo* at multiple defined DSBs. We identified a preferred sequence motif and related DNA meltability and bending profile for MRX nicking, indicating local DNA melting or kinking as an important step for endonucleolytic cleavage *in vivo.* Moreover, we find that the Ku complex and nucleosomes guide MRX nicking near and further away from DSB ends, respectively. We also observed that MRX nicking is mildly impeded by transcription, while heterochromatin does not represent a barrier to MRX activity. These findings reveal mechanistic details of the MRX nicking reaction *in vivo* and elucidate how resection initiates in the chromatin context.

Results

Monitoring Mre11-Rad50-Xrs2 (MRX) nicking at nucleotide resolution

We adapted the S1-seq protocol, previously used to characterize meiotic DSB end resection [27], to map MRX nick sites in mitotic cells quantitatively and at single-nucleotide resolution (Figure 1A). We arrested yeast cells in the G2/M cell cycle stage, where Sae2 phosphorylation is high and supports efficient MRX nicking, and then generated 21 defined DSBs in the yeast genome using our previously developed SrfI site-specific endonuclease expression system [28]. To preserve the 5’ ends produced by MRX incision, we needed to prevent further processing by long-range resection factors (Figure 1A). In principle, this could be achieved using *exo1*Δ *sgs1*Δ strains, where both long-range resection pathways are inactive. However, the *exo1*Δ *sgs1*Δ double deletion confers a strong growth defect, reduces DSB formation kinetics (Figure S1A), and leads to synthetic lethality when MRX activity is impaired [17]. To circumvent these shortcomings, we combined an *EXO1* deletion with conditional Sgs1 and Dna2 nuclear depletion using the anchor-away method [29]. Quantitative PCR (qPCR)-based resection assays confirmed tight long-range resection suppression, while short-range resection was unaffected, unless the *mre11-H125N* nuclease-dead allele was incorporated (Figure 1B and S1A). We then mapped MRX nick sites using the S1-seq method, which detects DSBs, nicks, and ssDNA/double-stranded DNA (dsDNA) junctions [27,30]. To map nick sites quantitatively, we employed unique molecular identifiers (UMIs) in the adapters [31]. At some SrfI sites, cutting was slow and incomplete for an extended period of time (Figure S1B) [28], when probably only one of the two sister chromatids was cleaved in many cells. To prevent the formation of subsequent sister chromatid recombination intermediates, which would generate MRX nicking-independent S1-seq signals [27], we deleted *RAD51* in all yeast strains analyzed by S1-seq.

Before DSB induction, negligible S1-seq coverage around DSB sites confirmed the tight regulation of SrfI expression (Figure 1C and Figure S1C). Upon DSB induction, we detect highly reproducible S1-seq coverage around break sites (Figure 1C and D). Reads mapped to the bottom and top strand upstream and downstream of breaks, respectively, as expected [27]. Importantly, in the *mre11-H125N* nuclease-dead strain, S1-seq coverage was mostly restricted to DSB sites, confirming that our method detected MRX-catalyzed resection (Figure 1C and S1D). We also detected DSB-independent S1-seq coverage at expected sites, such as ribosomal DNA repeats and mitochondrial DNA, where replication-associated ssDNA can be processed into library molecules (Figure S2). We conclude that combined long-range resection suppression and S1-seq reliably detects *in vivo* MRX nicking.

Over time, S1-seq coverage spread away from DSBs, consistent with multiple cycles of nicking (Figure 1C and E, Figure S1E–F). Interestingly, the spread of nicking slowed down over time (Figure S1G). In a previous study with long-range resection-proficient yeast strains, the presence of multiple DSBs reduced resection kinetics, probably by saturating the resection machinery [32]. We therefore asked if the observed slowdown in MRX nicking was due to a titration effect by the multiple DSBs. We found comparable MRX-mediated resection at a single DSB in the presence or absence of 20 additional DSBs (Figure S1H). This indicates that the MRX activity in mitotic *S. cerevisiae* cells is sufficient to process at least 21 DSBs simultaneously and suggests that the previously reported reduction in resection speed is due to limited capacity of the long-range resection machinery. The observed slowdown in the spread of MRX nicking could be due to other mechanisms, such as the recently reported inhibitory effect of the 9-1-1 DNA damage clamp on MRX-catalyzed end resection [33].

The Ku complex guides DSB-proximal MRX nicks

We detected the most DSB-proximal (“closest”) MRX nicks as near as 30 nt from DSB ends (Figure 2A). *In vitro*, the DSB end-binding Ku complex has been shown to stimulate and direct MRX nicking 30-35 nt from DSB ends [13,14,20]. We therefore hypothesized that the position of the closest MRX nicks in our *in vivo* data depended on Ku. Indeed, upon *YKU70* deletion, we detected a shift of the closest MRX nick sites to ca. 20 nt from the break ends. The extent of this shift is consistent with Ku occupying 14-18 bp at DSB ends, as deduced from structural studies [34–36]. To test if Ku alone is sufficient to guide MRX cleavage, we used reconstituted *in vitro* assays with purified yKu70-yKu80 complex, MRX, phosphorylated Sae2 (pSae2), and a 5’-end labeled plasmid-length substrate. Consistent with the *in vivo* data, the closest MRX nicks shifted further away from the DSB end when Ku was included in the reaction (Figure 2B). Higher Ku concentrations led to more Ku loading onto the DNA substrate but did not shift the closest MRX nicks further away from the DSB end (Figure 2B and C). However, nicking was slightly reduced for the highest Ku concentrations, as reported previously[13].

We noticed increased S1-seq signal within the first 5 nt from DSBs upon *YKU70* deletion (Figure 2A). As ss/dsDNA junctions with 5’ overhangs would also be detected with S1-seq, this signal probably derived from increased MRX exonuclease activity acting on the 3’-terminated DSB ends in the absence of Ku, as previously observed *in vitro* [13,14]. Thus, the Ku complex protects the 3’ ends at DSBs against Mre11 exonuclease-mediated degradation and guides MRX nicking on 5’ strands *in vivo*.

MRX preferentially nicks a specific sequence motif

Regions of high and low S1-seq coverage were reproducibly detected around DSBs (Figure 1C), which we interpreted as heterogeneous MRX nicking. We hypothesized that this heterogeneity reflected the influence of the local sequence and chromatin context on MRX cleavage *in vivo.* We set out to characterize these influences by leveraging the millions of observed nicking events and the single-nucleotide resolution and quantitative nature of our method. To determine if MRX nicking has a sequence preference, we retrieved the nucleotide sequence surrounding all nick sites and calculated S1-seq score-weighted averages (Figure 3A). The identified sequence motif indicated that MRX cleaves DNA preferentially 5’ of C, and to a lesser extent G, embedded in an AT-rich sequence (Figure 3B). Interestingly, this sequence was mostly rotationally symmetric around the central C or G in a region of ca. ±20 nt from the nick site. Upon further inspection, preferential cleavage 5’ of C was also evident in recently published data of MRX nicking in the vicinity of a single DSB in mitotic cells and in meiotic resection data (Figure S3A and B) [27,37].

To test if the observed sequence preference reflects an inherent feature of the MRX complex, we performed nuclease assays with purified MRX-pSae2 *in vitro.* We used a DNA substrate consisting of As and Ts with or without positioned Cs or Gs (Table S1). We anticipated that MRX nicking might not only be influenced by the presence of Cs or Gs, but also by the specific AT sequence context. Thus, we evaluated MRX nicking on both the top and the bottom strand of each substrate, where the positioned Cs and Gs are flanked by different AT sequences (see Table S1 for details). In agreement with the *in vivo* data, MRX-pSae2 nicking was enhanced when Cs or Gs were present in the DNA substrate (Figure 3C and D), and some product sizes were consistent with nicking at these positioned bases (Figure 3E). We observed that Cs stimulated nicking the most on the bottom strand, while Gs had the strongest stimulatory effect on the top strand (Figure 3C and D). We conclude that Cs or Gs stimulate the DNA cutting efficacy, and the surrounding DNA sequence additionally influences where and how efficiently MRX nicks DNA.

Mechanistically, improved nicking of the C- and G-containing substrates could be due to increased substrate binding and/or nicking by the MRX complex. To distinguish between these possibilities, we performed electrophoretic mobility shift assays with nuclease-inhibited ATP-γ-S-bound Mre11-Rad50 complex and the AT-rich substrate containing or lacking Cs (Figure 3F and G). Both substrates were bound equally well. Thus, the sequence preference results from enhanced nicking rather than improved substrate binding.

Given that both the Ku complex and the sequence composition of the DNA substrate influenced MRX nicking, we asked how these two effects would interact. We incubated an AT-rich substrate containing or lacking positioned Cs with purified MRX-pSae2 and a concentration series of Ku. We observed that the presence of Cs increased nicking for all Ku concentrations (Figure S3C and D). Moreover, Ku improved MRX nicking for both substrates in a concentration-dependent manner, except for the highest Ku concentration, which is consistent with a previous report [13]. Overall, we observed an additive effect of sequence- and Ku-mediated stimulation of MRX nicking. In agreement with our *in vivo* findings and our *in vitro* cleavage assays with the plasmid-length substrate (Figure 2B), the nick site locations changed slightly upon the addition of Ku (Figure S3C). We conclude that both DSB end-binding proteins and the local sequence context determine MRX nicking efficiency and location.

MRX preferentially cleaves DNA with a specific melting temperature profile

Previous *in vitro* findings suggest that the MR complex locally melts dsDNA prior to 5’-specific incision [21,24]. If this model is correct and applies also to the *in vivo* situation, local DNA meltability might influence MRX nicking efficiency. We calculated melting temperature profiles around each detected nick site and derived an S1-seq score-weighted average (Figure 4A). We found a preference for a low melting temperature around the nick sites, consistent with the AT-rich sequence motif (Figure 4B and S4A). Interestingly, besides a preference for a generally low melting temperature, we identified a specific profile with a melting temperature peak and valley ca. 5 nt upstream and 5 nt downstream of the nick site, respectively, coinciding with elevated and reduced GC fractions in the sequence motif (Figure 3B and 4B).

To test if the derived melting temperature preferences were MRX-inherent properties, we performed *in vitro* nuclease assays using DNA substrates with low, medium, or high overall melting temperature and containing or lacking the identified peak-valley profile (Figure S4B). Consistent with the *in vivo* data, we found reduced nicking with increasing overall melting temperature and a mildly stimulating effect of the profile (Figure 4C and D).

A recent cryo-electron microscopy (cryo-EM) study of the *E. coli* SbcCD (MR) complex in the endonuclease state implies DNA kinking rather than DNA melting near the Mre11 nuclease site [25]. We asked if DNA kinking might likewise be involved in the *S. cerevisiae* MRX nicking reaction. We calculated DNA shape features around all MRX nick sites detected *in vivo* and derived S1-seq score-weighted averages[38]. We observed an MRX nicking preference at DNA sequences with a local peak of the minor groove width (MGW) (Figure S4C), which has been associated with improved DNA bending or kinking[39]. We noticed that our *in vitro* substrates differed not only in their melting temperature profiles, but also in their MGW profiles (Figure S4D–F). In contrast, our *in vitro* substrates to check the MRX nicking sequence bias differed slightly in their melting temperature profiles, while their MGW profiles were very similar (Figure S3E–F). Thus, our findings suggest that DNA meltability influences MRX nicking, but our results are also consistent with an influence of DNA kinking.

Nucleosomes guide MRX nicking

Since MRX initiates end resection in the context of chromatin in cells, we next set out to study how chromatin features impact MRX nicking. We first asked if nucleosomes might determine MRX nick sites. To correlate nucleosome positions and MRX cleavage, we prepared MNase-seq and S1-seq libraries from the same samples. We reproducibly observed a decrease of MNase-seq coverage concomitant with the spread of S1-seq coverage from DSBs, consistent with resection-mediated depletion of dsDNA substrate for MNase-seq library preparation (Figure 5A and S5A). S1-seq peaks showed a mild level of anti-correlation with MNase-seq peaks at individual DSBs as well as when averaged over all DSBs (Figure 5A and B).

To test for causality, we perturbed nucleosome occupancy around a DSB and analyzed the impact on MRX cleavage. We employed *pho4*Δ and *pho4-SA1234PA6* (*pho4-SA*) alleles, which have previously been shown to yield high or low nucleosome occupancy, respectively, at several gene promoters [40,41], and we inserted an SrfI cut site at one of these, the *PHO5* promoter. We observed the previously reported change in nucleosome occupancy and associated *PHO5* expression using MNase-seq and a Pho5 biochemical activity assay, respectively (Figure 5C and S5B) [41]. Upon DSB formation, S1-seq coverage spread slightly faster through the *PHO5* promoter region resulting in a mildly elevated signal at the start of the *PHO5* coding sequence (CDS) in the nucleosome-depleted condition (*pho4-SA*) as compared to the condition with positioned nucleosomes (*pho4*Δ) (Figure 5C). We noticed an overall reduced S1-seq coverage for the *pho4-SA* allele, which we attribute to reduced DSB formation, as seen in a qPCR-based assay (Figure S5C). To confirm the shift in MRX nicking quantitatively, we used a qPCR-based resection assay. Consistent with the S1-seq data, we found mildly increased resection near the *PHO5* CDS start in the *pho4-SA* strain as compared to the *pho4*Δ strain, while there was no difference nearer to the DSB (Figure 5D). Thus, nucleosomes modestly guide the location of MRX nicks in mitotic cells.

Chromatin remodelers are mostly dispensable for MRX nicking

Several chromatin remodelers support DSB end resection in the chromatin context [42]. Among them, the RSC complex, SWI/SNF complex, and Chd1 have been reported to promote resection near DSB ends [43–46]. However, as these studies were carried out in long-range resection-proficient strains, it is unclear whether the remodelers enhance MRX nicking itself or affect downstream processes, such as long-range resection factor recruitment or activity. To address this question, we monitored MRX cleavage activity in our long-range resection-suppressed strains upon deletion of *RSC2, SNF5*, or *CHD1* using a qPCR-based assay (Figure 5E and S5D). All three deletions resulted in a slight reduction of MRX-mediated resection with *rsc2*Δ showing the most pronounced effect.

Chromatin remodelers might act redundantly to facilitate end resection. Indeed, a recent study reported a strong long-range resection defect upon simultaneous inactivation of Sth1 and Snf2 [47], which are the catalytic subunits of the RSC and SWI/SNF complex, respectively. As a *STH1* deletion is lethal and a *SNF2* deletion results in a strong growth defect, a conditional auxin-inducible degradation system was employed. We wondered if combined Sth1 and Snf2 inactivation would also impede MRX nicking. Taking advantage of the anchor-away system in our strains, we achieved tight conditional depletion of Sth1 and Snf2, as confirmed by the expected viability and growth defects (Figure S5E). We monitored MRX nicking with a qPCR-based assay and found that individual depletion of Sth1 or Snf2 resulted in slightly increased or reduced nicking, respectively, while simultaneous depletion of both Sth1 and Snf2 did not change MRX-mediated resection (Figure 5F and S5F). These results indicate that the chromatin remodelers RSC, SWI/SNF, and Chd1 do not considerably influence MRX nicking.

MRX nicking is indistinguishable in euchromatin and heterochromatin

We next asked if MRX cleavage would differ in euchromatic versus heterochromatic genome regions. The yeast genome contains few heterochromatic regions [48] and none of the SrfI sites was located near to any of them. Therefore, we engineered a DSB formation site next to a heterochromatic region, the transcriptionally silenced mating-type cassette *HMR* (Figure 5G). We unsilenced the locus by deleting silencer seed sequences and found release of transcriptional suppression, as expected (Figure S5G). Both, S1-seq coverage and a qPCR-based resection assay showed no difference between MRX nicking at the silenced and unsilenced locus (Figure 5G, H, and S5H). We conclude that heterochromatin does not represent a barrier to MRX nuclease activity. Consistent with this observation, DSBs in heterochromatin in *Drosophila melanogaster* and human cells are resected [49,50].

Transcription mildly impedes MRX nicking

To address how MRX nicking interconnects with other DNA transactions, such as transcription, we derived transcription levels around SrfI sites using previously published RNA-seq data [51]. The employed data had been obtained from yeast cells of the same genetic background and in the same cell cycle stage as our cells. In addition, we confirmed transcript levels near several SrfI sites by reverse transcription-qPCR (Figure S6A and B). We observed instances where the S1-seq level sharply dropped at the transition between highly and lowly transcribed regions (Figure 6A). Moreover, when averaging over multiple DSBs, S1-seq coverage spread slower in transcribed than in untranscribed regions (Figure 6B and S6C). A previous report showed that resection through a promoter inactivates downstream transcription [52], which might abrogate a repressive effect of transcription on resection if both processes are co-oriented. Consistently, we found faster S1-seq spreading, when it was co-oriented with the transcription direction compared to a converging orientation (Figure 6C and S6D).

We considered if transcription *per se* or if features associated with transcribed and untranscribed regions impact MRX nicking. DSB formation kinetics did not generally differ between transcribed and untranscribed regions (Figure S6E). However, transcribed and untranscribed regions tended to differ in the prevalence of the preferred sequence motif and the local melting temperature (Figure S6F and G), which is consistent with untranscribed regions corresponding to AT-rich promoter and terminator sequences. To directly test if transcription *per se* influences incisions by MRX, we modulated transcription levels at a DSB. We employed a fluorescent reporter gene followed by a DSB formation site. The reporter gene lacked a promoter or contained the strong *TDH3* promoter to achieve low or high transcription, respectively. Using flow cytometry, we detected background-level or strong fluorescent protein expression, respectively, as expected (Figure S6H). Upon DSB induction, S1-seq showed that nicking spread slightly faster in the promoter-less gene as compared to the *TDH3* promoter-containing gene (Figure 6D). As DSB formation efficiency differed slightly between the genes (Figure S6I), we also quantified resection with a qPCR-based assay and confirmed slightly enhanced resection for the promoter-less gene compared to the *TDH3* promoter-driven gene (Figure 6E). At a second reporter gene series, where a DSB was created within the gene body, we again observed mildly enhanced resection of the untranscribed versus transcribed reporter using a qPCR-based assay, although this behavior was not apparent in the S1-seq data (Figure S6J–L). We conclude that transcription mildly impedes MRX nicking.

Discussion

Here we show that DSB resection initiation by the MRX endonuclease is influenced by the local sequence and chromatin context. We identified a sequence motif and associated melting temperature profile that are preferentially nicked by MRX. These preferences are consistent with an MRX cleavage mechanism that involves local DNA melting or kinking. Moreover, we observed that Ku and nucleosomes determine MRX nick site locations, while transcription impedes nicking.

We developed an assay to map MRX nick sites quantitatively and at single-nucleotide resolution. Using this assay and complementary *in vitro* experiments, we found that the location of the most DSB-proximal (“closest”) nick sites depends on the Ku complex. Specifically, the closest nick sites shifted further away from the DSB ends in the presence of Ku. Interestingly, loading more Ku complexes on the DNA substrate did not increase the shift to more DSB-distal sites in the *in vitro* assays. This indicates that only the DSB-proximal Ku complex guides MRX nicking, even if additional Ku complexes are bound further away from the DSB. We note that this might be different for the mammalian Ku complex, where cooperative DNA binding has been reported, which could lead to stable assembly of several Ku complexes at DSB ends [53]. Moreover, binding of DNA-PKcs to Ku has been reported to stimulate MRN nicking *in vitro* and to alter the location of nick sites [15].

The quantitative nature and single-nucleotide resolution of our method allowed us to identify a sequence preference for MRX activity *in vivo.* Interestingly, the identified sequence motif contains a mostly palindromic region centered at the nick site (Figure 3B). It is tempting to speculate that this reflects DNA binding by the MRX complex in a rotationally symmetric fashion, consistent with the complex's symmetric dimer of heterotrimer-configuration. While no crystal structure of the *S. cerevisiae* MRX complex is available to date, structures of DNA-bound complexes from other species support this DNA binding configuration [21–23].

The identified sequence motif indicates that MRX nicks preferentially 5' of Cs in an AT-rich sequence context. This preference was not due to improved DNA binding, but rather enhanced MRX endonuclease activity when tested *in vitro.* A bias for cleavage 5' of Cs was also observed for Mre11-dependent resection at a hotspot located 60-70 bp from a single site-specific DSB in yeast, consistent with our findings [37]. We speculate that MRX interacts with the base immediately downstream of the nick site either during the transition to the endonucleolytically active conformation or within the Mre11 active site. We anticipate that the details of this interaction will be clarified by future molecular structures of the eukaryotic MR complex in its nicking state, which are not yet available.

As an alternative to base-specific interactions, the identified sequence motif might also relate to shape or physical properties of the DNA substrate that support MRX nicking. Indeed, we identified a preferred DNA meltability profile for MRX cleavage, which relates to the identified sequence preference. Nicking was enhanced at DNA sequences with an asymmetric melting temperature profile (Figure 4B). Interestingly, this preferred profile is consistent with previously published *in vitro* nuclease assays using hairpin substrates and the *S. cerevisiae* MR or *Escherichia coli* MR (SbcCD) complex, where nicking was observed at the transition between paired and unpaired DNA (Figure S4G) [54,55]. This indicates an evolutionary conserved MR preference to cleave at DNA junctions.

Moreover, MRX nicking was enhanced at sequences with overall low melting temperature. This observation is consistent with early biochemical and biophysical studies, which suggested that the MR complex locally melts dsDNA to insert the 5' strand into the Mre11 active site [21,24,26,56,57]. However, a recent cryo-EM structure of the *E. coli* MR complex in the endonuclease state shows no evidence for DNA melting and instead DNA is kinked near the Mre11 active site [25]. Consistently, we found that MRX nicking *in vivo* was preferred at sequences supporting DNA kinking (Figure S4C). Thus, both DNA melting and kinking could facilitate MRX nicking. As our *in vitro* substrates often differed in both DNA melting and kinking, we cannot clearly discriminate between these possibilities. We anticipate that future structural, biochemical, and biophysical studies will reveal the relative contributions of these DNA features resulting in efficient, strand-specific MRX nicking in the vicinity of DSBs.

We mapped nicking at DSBs at multiple genomic locations, which allowed us to study the impact of local chromatin context on MRX endonuclease activity. We found a weak anti-correlation between nucleosome occupancy and MRX nicking, which can be interpreted as a mild guiding effect of nucleosomes on MRX cleavage positions. However, as both nucleosome positions and nick sites were determined using population-based methods (MNase-seq and S1-seq, respectively), we cannot rule out that there is a stronger guiding effect for each individual nicking event, which is obscured by the population heterogeneity. Future single-molecule experiments will be necessary to investigate the interplay between nucleosomes and MRX nicking at high precision. In any case, our data indicate that MRX nicking occurs preferentially in linker regions between nucleosomes, which is consistent with previous reports for meiotic cells and *in vitro* assays [14,27].

Several chromatin remodelers have been implicated in DSB end resection [42] and the RSC complex, the SWI/SNF complex, and the Chd1 protein have been reported to facilitate resection near to DSBs [43–46]. We found only a mild MRX nicking defect when inactivating these remodelers individually or the RSC and SWI/SNF complexes simultaneously. This suggests that the previously reported resection dependence on chromatin remodelers is due to effects on long-range resection rather than MRX nicking. Previous studies reported a reduced MRX recruitment to DSBs in the absence of chromatin remodelers [43,44,46]. Our data suggest that the reduced MRX level supports efficient nicking, while it might result in a reduced recruitment of long-range resection factors [44,46]. Although we cannot rule out that other chromatin remodelers or their combination supports MRX nicking, the data presented here indicate that active chromatin remodeling might not be a major determinant of MRX cleavage activity. Notably, the MRN complex can bypass nucleosomes [20]. Therefore, it is in principle possible that MRX can nick downstream of a DSB-proximal nucleosome and, starting from this nick, resect back towards the DSB, thus, destabilizing the nucleosome. Further studies will be necessary to reveal how MRX nicking is restricted to regions near DSBs and how nicking and nucleosome dynamics interact. We also note that chromatin remodelers often serve multiple functions, among them transcription regulation [58,59]. As reduced transcription favors MRX nicking (see below), perturbing chromatin remodelers might also influence MRX nicking indirectly, and this could be the reason why we unexpectedly observed a slight increase in MRX nicking upon RSC inactivation.

In mammalian cells, DSBs in transcribed regions are preferentially resected and repaired by HR [60]. Concomitantly, DSBs trigger a DNA damage signaling-mediated local transcription shutdown in higher eukaryotes [61]. This complicates the analysis of whether transcription might influence resection. As a DSB-induced transcription shutdown is absent in budding yeast [52], we could directly evaluate if transcription influences resection initiation by MRX nicking and found an inhibitory effect. The observed effect was mild, which could be due to a generally small effect or a masking of a stronger effect due to heterogeneity in the population-based measurements (RNA-seq and S1-seq). In any case, transcription might counteract MRX nicking by steric hindrance or by generating R-loops, which could impede MRX nuclease activity, as shown for mammalian MRN [62]. Thus, one role for the DSB-triggered transcription shutdown in higher eukaryotes might be to support efficient MRN nicking, which is essential for DSB end resection in these organisms.

Over time, MRX nicks were observed at increasing distances from DSBs, consistent with previous Southern blotting-based analysis of end resection in long-range deficient cells and *in vitro* observations with purified MRX-pSae2 [17,18,63,64]. Interestingly, MRX-dependent resection tracts formed 2 h after SrfI induction are of comparable lengths to those reported for meiotic cells (Mimitou et al., 2017), indicating similar MRX nicking activity in mitotic and meiotic chromatin.

It has been proposed that the spread of MRX nicking could be due to either stepwise extension by repetitive nicking or to single MRX nicking events at a greater distance from the DSB at later time points. The temporal evolution of the average S1-seq coverage distributions (Figure 1E) supports the model of stepwise nicking. Mechanistically, this process could rely on MRX-mediated ssDNA overhang generation followed by RPA binding, which stimulates further nicking [13,14,63]. A recent publication also indicates MRX oligomerization at DSB ends as a potential mechanism for stepwise MRX cleavage [64]. Independent of the mechanistic details, we note that MRX nick site spreading will probably be of minor importance in a long-range resection-proficient setting. Future work will reveal how many MRX nicks occur before long-range resection takes over and how this might vary depending on the sequence and chromatin context.

Overall, our data show that MRX cleavage is governed by local DNA sequence and associated physical properties. These findings support a nicking mechanism, where the MRX complex locally changes DNA conformation for nicking. In contrast, MRX nicking is only mildly influenced by local chromatin features, such as nucleosome occupancy, chromatin state, and transcription, highlighting the versatility of MRX to initiate resection in multiple genomic locations. Our findings might also support DSB-based genome engineering applications by identifying target sites permissive for efficient MRX/N-mediated resection initiation.

Limitations of the study

We suppressed long-range resection to be able to detect MRX nicking events. We cannot rule out that the observed MRX nicking behavior under this condition is different from a long-range resection-proficient setting, since we do not know if long-range resection factors influence MRX nicking. Additionally, long-range resection would probably take over after the first or a few MRX nicks, such that MRX nicking further away from the DSB end would not occur. We do not know if, in a long-range resection-suppressed setting, MRX nicking near a (Ku-bound) DSB end and further away from a DSB (near the junction of [RPA-coated] ssDNA and dsDNA) is mechanistically identical. Our studies indicate that DNA sequence and DNA sequence-associated features (melting temperature and probably DNA shape) influence MRX nicking. As these properties are intimately linked, we do not know what their relative contribution to the observed influence is. It is important to note that S1-seq does not detect which DNA strand is nicked and resected. However, *in vitro* and *in vivo* data show that nicking is restricted to the 5’ strand for the *S. cerevisiae* MRX complex [10,17].

STAR Methods

RESOURCE AVAILABILITY

Lead Contact—Further information and requests for resources and reagents should be directed to and will be fulfilled by the Lead Contact, Lorraine Symington (lss5@cumc.columbia.edu).

Materials Availability—Plasmids and yeast strains generated in this study are available from the Lead Contact without restriction, except for plasmids and yeast strains containing the SrfI endonuclease gene, which require a completed Materials Transfer Agreement.

Data and Code Availability

- S1-seq and MNase-seq data have been deposited at SRA and are publicly available as of the date of publication. The accession number is listed in the key resources table. Original gel images have been deposited at Zenodo and are publicly available as of the date of publication. The DOI is listed in the key resources table. This paper analyzes existing, publicly available data. The accession numbers for the datasets are listed in the key resources table.
- All original code has been deposited at Zenodo and is publicly available as of the date of publication. The DOI is listed in the key resources table.
- Any additional information required to reanalyze the data reported in this paper is available from the lead contact upon request.

EXPERIMENTAL MODEL AND SUBJECT DETAILS

Saccharomyces cerevisiae strains were thawed from frozen stocks and grown at 30°C using standard genetic practices.

Method Details

Yeast strains and plasmids: The key resource table lists all yeast strains and plasmids used in this study. We cloned plasmids using enzymes from New England Biolabs (NEB) and we used *Escherichia coli* DH5α for plasmid amplification. Plasmid sequences were verified by control digests and Sanger sequencing (Genewiz). All yeast strains were of W303 genetic background with corrected the *rad5-535* allele (to wild-type *RAD5*). We derived genetic modifications by plasmid integration [67], genetic crosses, and CRISPR/Cas9-mediated genome engineering [68]. Plasmid and strain construction details are available upon request.

Yeast media and culture conditions: We grew yeast cells in YPD media containing 1% yeast extract, 2% peptone, and 2% glucose. Solid media additionally contained 2% agar. Yeast cells were grown at 30°C. Liquid cultures were shaken vigorously. Prior to DSB induction, we arrested yeast cells in G2/M by adding 1% DMSO and 20 µg/ml Nocodazole (diluted from a DMSO stock) and culturing for 1.5 generation times. Visual inspection confirmed that ≥90% of cells showed G2/M morphology. We then anchored away Sgs1-FRB and Dna2-FRB by adding 1 µg/ml Rapamycin (diluted from a DMSO stock) and culturing for 1.5 hours. Finally, we induced DSB formation by adding 2 μM β-Estradiol (diluted from an ethanol stock).

Quantitative PCR (qPCR)-based resection assay: We measured resection using a qPCR-based assay [69]. We collected ca. 10^8 G2/M-arrested and Rapamycin-treated cells, added 0.1% sodium azide, pelleted by centrifugation, and washed with TE (10 mM Tris, 1 mM EDTA, pH 8) containing 0.1% sodium azide. We extracted genomic DNA using the MasterPure Yeast DNA Purification Kit with RNase treatment according to the manufacturer's instructions. We diluted the genomic DNA to ca. 2.5 ng/μl in 1x CutSmart Buffer and digested about half of this solution with 40 U/μg DNA of the appropriate restriction enzyme (see Table S2 for amplicon-restriction enzyme correspondence). Per sample and amplicon, we prepared triplicates containing 11 ng of digested or undigested genomic DNA, 300 nM of each forward and reverse primer (listed in Table S2), and 1x SsoAdvanced Universal SYBR Green Supermix in a total volume of 10 μl and analyzed them on a CFX384 Real-Time System with 10 minutes initial denaturation at 95°C, followed by 40 cycles of 1 minute denaturation at 95°C and 1 minute annealing and extension at 58°C. The fraction of ssDNA f_{ssDNA} at the restriction enzyme recognition site was calculated according to [70] and [71] with the formula

$$f_{ssDNA} = \frac{2}{\left(E_{target}\left(C_{q\,digested} - C_{q\,undigested}\right) + 1\right) \cdot f_{DSB}}$$

where E_{target} is the primer efficiency of the target amplicon (spanning the restriction site) and $C_{q\ digested}$ and $C_{q\ undigested}$ are the quantification cycles for digested and undigested genomic DNA, respectively. f_{DSB} is the fraction of formed DSBs, from where resection generates the ssDNA at the target amplicon, and can be calculated with the formula

$$f_{DSB} = 1 - \frac{E_{DSB}\left(C_{q\,t0} - C_{q\,t}\right)}{E_{ADH1}\left(C_{q\,t0} - C_{q\,t}\right)}$$

where E_{DSB} and E_{ADH1} are the primer efficiencies of the amplicon spanning the DSB site and of the *ADH1* reference amplicon, respectively, and $C_{q\ t0}$ and $C_{q\ t}$ are the quantification cycles for the sample before DSB induction and at time *t* after DSB induction, respectively. Analysis scripts can be found at https://doi.org/10.5281/zenodo.7508119.

S1-seq library preparation: To prepare S1-seq libraries [72], we collected ca. $2 \cdot 10^9$ G2/M arrested and Rapamycin-treated cells grown in 100 ml YPD and embedded them into 10 low melting point (LMP) agarose (Certified Low Melt Agarose) plugs. Upon solidification, we incubated each plug individually with 500 μl of buffer or reaction mix solutions in 2 ml tubes. All enzymatic reactions were proceeded by plug equilibrations with the reaction buffer four times for 30 minutes. We used siliconized G-Tubes (BIO PLAS) when possible to minimize DNA loss. We incubated the plugs with solutions 2 and 3 [72]. Plugs were equilibrated in S1 Nuclease buffer (0.5 M Sodium acetate, 2.8 M NaCl, 45 mM $ZnSO_4$, pH 4.5) and incubated with 10 U S1 Nuclease for 45 minutes at 25°C. To polish DNA ends, we equilibrated with NEBuffer 2.1 containing 100 μM dNTPs and incubated with 10 U T4 DNA Polymerase for 90 minutes at 12°C. To A-tail, we equilibrated in NEBuffer 2 containing 100 µM dATP and incubated with 10 U Klenow Fragment 3’-5’exo$^-$ at 37°C for 30 minutes. We annealed biotinylated P5 adapters with a 3’-T overhang (see Table S3 for adapter sequences) in Annealing Buffer (10 mM Tris-HCl, 50 mM NaCl, 1 mM EDTA, pH 7.5) by heating to 95°C for 5 minutes and slowly cooling to 4°C over the course of 2 hours. We submerged plugs in 50 µl T4 DNA Ligase buffer containing 1 µM adapter and 400 U T4 DNA Ligase and incubated at 16°C overnight. To retrieve DNA from plugs, we equilibrated with β-Agarase I buffer and digested agarose with 1 U β-Agarase I (NEB) per 200 µl molten sample for 1 hour at 42°C followed by phenol/chloroform extraction and ethanol/ammonium acetate precipitation. We dissolved the precipitated DNA in 50 µl TE (10 mM Tris, 1 mM EDTA, pH 8) buffer, added 10 µl 6x Gel loading dye without SDS containing 60x SYBR Gold Nucleic Acid Gel Stain, ran the solution on a 1xTAE 1% LMP agarose gel, and excised high molecular weight DNA on a blue light screen. β-Agarase I digest, phenol/chloroform extraction, and ethanol precipitation were performed as above. We resuspended the DNA in 130 µl TE and subjected it to shearing in Covaris microTUBEs using a Covaris S220 Ultrasonicator with 2 minutes treatment time, 10% duty factor, 175 W peak incident power, and 200 cycles per burst. We confirmed appropriate fragmentation by subjecting 100 ng of sonicated samples to agarose gel electrophoresis and post-run Ethidium bromide staining. To remove unligated adapters from the sonicated DNA solutions, we performed three subsequent cleanups with SPRI beads (prepared according to dx.doi.org/10.17504/protocols.io.bnz4mf8w) in a 1:1 ratio with the DNA volume following the instructions for AMPure XP beads (Beckman Coulter). Upon capture of biotinylated fragments on Dynabeads M-280 Streptavidin, we repaired sheared ends with the NEBNext end repair module according to the manufacturer’s instructions. We subsequently A-tailed using the conditions as above. We annealed P7 adapters with a 3’-T overhang as above (see Table S3 for adapter sequences). We ligated the captured DNA fragments with 1 µM adapter and 400 U T4 DNA Ligase at 20°C for 3.5 hours. After washing, we resuspended the beads in 30 µl 10 mM Tris pH 8 per sample. We used 3x 10 µl bead resuspension in separate PCR amplification reactions with the KAPA HiFi PCR Kit according to the manufacturer’s instructions (see Table S3 for library amplification primer sequences). We amplified with 12 cycles, checked for visible products by Ethidium bromide agarose gel electrophoresis, and ran additional PCR cycles if necessary. We performed a 1:1 SPRI bead cleanup, quantified the DNA concentration with the Qubit Flex system, analyzed the fragment size distribution with a Bioanalyzer High Sensitivity DNA chip (Agilent), and deep-sequenced pooled libraries using the NextSeq 500 System (Illumina) with 150 cycle single end reads (adapter version 1, see note below) or paired end reads (125 and 25 cycles for first and second read, respectively; adapter version 2 and 3).

Note: During the course of this study, we optimized our adapter design for improved output of library reads and ease of data analysis (see Table S3 for adapter sequences). We used a unique molecular identifier (UMI) sequence in one of the adapters to distinguish if reads with identical mapping originated from different input molecules or PCR amplification of the same input molecule. This allowed us to map nicking events quantitatively. The UMI sequence had to be followed by a linker sequence, such that the adapter finished with an annealed, ligatable end. In the first version of our adapter design, the UMI and linker sequence are located at the 3’ end of the P5 adapter. The constant sequence of the linker resulted in identical bases being read across the flow cell during cycles 13-22 of the first read. This required a high PhiX spike-in (20%) to counteract low run performance and data quality, as balanced base fractions are critical during the first 25 cycles on the NextSeq 500 System.

In the second adapter design version, we relocated the UMI and linker sequence to the P7 adapter. This alleviated the need of a high PhiX spike-in. However, the identical bases during cycles 13-22 of the second read resulted in poor data quality and many discarded reads when base calls were done with the bcl2fastq software using standard settings (e.g., as done automatically on BaseSpace upon run completion). This required rerunning bcl2fastq software with adjusted settings (see section “Deep sequencing data analysis” below for details).

In the third adapter design version, we used a mix of P7 adapters, where the UMI was followed by one of four different linkers, resulting in balanced base fractions throughout all sequencing cycles.

Preparation of DNA substrate for *in vitro* assays: The 70-bp and 166-bp oligonucleotide substrates used for the endonuclease assays were obtained by annealing 3’-labeled oligonucleotides with a two-fold excess of the complementary strand (see Table S1 for oligonucleotide sequences). The 3’-labeling was performed with Terminal Deoxynucleotidyl Transferase (NEB) and [α-^{32}P]dCTP (PerkinElmer) according to manufacturer’s instructions and purified on Micro Bio-Spin P-30 Gel Columns (Bio-Rad). For the generation of the 5’ labeled plasmid-length substrate, oligonucleotide PC210 (Table S1) was labeled at the 5’ end using T4 polynucleotide kinase (New England Biolabs) and [γ-32P]ATP (PerkinElmer) according to the manufacturer’s instructions and annealed with a two-fold excess of PC211. The labeled dsDNA was then integrated in the pAttP-S vector using ΦC31 integrase[73].

Protein purification: The *S. cerevisiae* Mre11-Rad50-Xrs2 and Mre11-Rad50 complexes were expressed in *Spodoptera frugiperda Sf9* cells using baculoviruses produced with pTP391 expressing His-tagged Mre11, a kind gift from Tanya Paull (University of Texas at Austin, Austin, TX), pFB-Xrs2-3xFLAG expressing Xrs2 tagged with 3xFLAG (omitted for the MR complex) and pFB-Rad50 expressing untagged Rad50. pFB-Xrs2-3xFLAG was prepared from pTP694, a kind gift from Tanya Paull (University of Texas at Austin, Austin, TX) by PCR with primers Xrs2-3XFLAG_fw (gactacaaggaccacgacatcGACTACAAGGACGACGACG, 5’ to 3’) and Xrs2-3XFLAG_rev (accatcatgatctttgtaatcGCCTCCTTTTCTTCTTTTGAAC, 5’ to 3’). The MRX complex was purified by NiNTA and FLAG affinity chromatography [10]. The MR complex was purified by NiNTA affinity chromatography followed by ion-exchange chromatography on an AKTA system [74]. Phosphorylated Sae2 (denoted pSae2) was expressed in *Sf*9 cells using the pFB-MBP-Sae2-His vector expressing MBP and His-tagged Sae2 in the presence of phosphatases inhibitors [75]. The purification was carried out by amylose and NiNTA affinity chromatography. The MBP tag was removed by incubation of the protein with PreScission Protease before the NiNTA affinity purification step. The KU complex was expressed in *Sf*9 cells with pFB-MBP-YKU70-his and pFB-YKU80-FLAG constructs, coding for MBP- and

10xHis-tagged Yku70 and FLAG-tagged Yku80, respectively. The purification was carried out as described previously [13].

In vitro nuclease assays: Endonuclease assays (15 µl volume) were performed in a reaction buffer containing 25 mM Tris-acetate pH 7.5, 1 mM dithiothreitol, 5 mM magnesium chloride, 1 mM ATP, 80 U/ml pyruvate kinase (Sigma), 1 mM phosphoenolpyruvate, 0.25 mg/ml bovine serum albumin (NEB) and 1 nM DNA substrate (in molecules). NaCl was added to a final concentration of 45 mM. 25 nM MRX and 200 nM pSae2 were added where indicated, and the reactions were incubated for 30 min at 30°C. For the reaction in the presence of protein blocks, 1 mM manganese chloride was supplemented to the reaction and no further NaCl salt was added to the reaction. The substrate was incubated with 30 nM Ku or monovalent Streptavidin (a kind gift from M. Howarth, University of Oxford) for 5 min at 30°C before addition of MRX and pSae2. Reactions were stopped by addition of 0.5 µl of 14–22 mg/ml proteinase K (Roche), 0.5 µl of 10% (w/v) sodium dodecyl sulfate and 0.5 µl of 0.5 M ethylenediaminetetraacetic acid (EDTA) followed by incubation for 30 min at 50 °C. Deproteinated samples were supplemented with equal volume of 2x loading dye (95% formamide, 20 mM EDTA, 1 mg/ml bromophenol blue) and separated by denaturing electrophoresis in 15% acrylamide gels containing 7 M urea. After separation, the gels were fixed in fixing solution (40% methanol, 10% acetic acid and 5% glycerol) for 30 min while shaking and dried on 3MM paper (Whatman), exposed to phosphor screen and imaged using a Typhoon imager (GE Healthcare). Endonuclease activity was obtained by calculating the percentage of endonuclease products compared to the amount of substrate in the control lane using ImageJ Software (version 1.53c).

Electrophoretic mobility shift assays: MR-DNA binding experiments were performed in binding buffer containing 25 mM Tris-acetate pH 7.5, 1 mM dithiothreitol, 5 mM magnesium chloride, 1 mM ATP-γ-S, 0.25 mg/ml bovine serum albumin (NEB) and 100 nM (in base pairs) DNA substrate. The indicated amount of protein was added, and the samples were incubated for 15 min at 30°C. After incubation, the reaction was supplemented with 5 µl of EMSA loading dye (50 % glycerol with Bromophenol Blue) and separated on a 6% polyacrylamide gel (TAE) on ice. Gels were dried on 17CHR paper (Whatman), exposed to phosphor screen and imaged with a Typhoon imager (GE Healthcare). DNA binding was obtained by calculating the percentage of unbound substrate compared with the control lane using ImageJ Software (version 1.53c).

Ku binding experiments were performed in binding buffer containing 25 mM Tris-acetate pH 7.5, 1 mM dithiothreitol, 5 mM magnesium chloride, 5 mM manganese chloride, 1 mM ATP, 0.25 mg/ml bovine serum albumin (NEB), 45 mM NaCl and 1 nM 5’-labeled plasmid-length DNA substrate. The indicated amount of protein was added, and the samples were incubated for 15 min at 30°C. After incubation, the reaction was supplemented with 5 µl of EMSA loading dye (50 % glycerol with Bromophenol Blue) and separated on a 0.6% agarose gel (TAE) at 4°C. The gel was dried on DE81 paper, exposed to phosphor screen and imaged with a Typhoon imager (GE Healthcare).

MNase-seq library preparation: Cells were collected and split for S1-seq (see above) and MNase-seq (micrococcal nuclease digestion with deep sequencing) library preparation.

We prepared MNase-seq libraries as previously described [59] with modifications. We used siliconized G-Tubes (BIO PLAS) when possible to minimize DNA loss. Briefly, we crosslinked ca. 10^9 G2/M arrested cells per sample with 1% formaldehyde for 5 minutes at room temperature. We quenched by the addition of 125 mM Glycine and incubated for 5 minutes at room temperature. We collected cells by centrifugation at 2000 g and 3 minutes at room temperature, resuspended in 1 M sorbitol, recollected by centrifugation as above, and discarded the supernatant. We snap-froze cell pellets in liquid nitrogen and stored at −80°C. We thawed and washed the pellets in 1 M Sorbitol, collected by centrifugation, discarded the supernatant, and resuspended the pellets in 1 ml Spheroplasting Buffer containing 1 M Sorbitol, 1 mM β-Mercaptoethanol, and 3 mg/ml Zymolyase 100T. We monitored the spheroplasting progress by resuspending 10 μl of the reaction mix in 1 ml 1% SDS solution and measuring the OD at 600 nm [76]. When the OD dropped below ca. 15% of the initial value (after ca. 15 minutes), we collected spheroplasts by centrifugation at 20,000 g for 30 seconds, and carefully washed twice with 1 M Sorbitol. We resuspended the spheroplasts in 1.5 ml MNase Digestion Buffer (1 M Sorbitol, 50 mM NaCl, 10 mM Tris pH 7.4, 5 mM $MgCl_2$, 1 mM $CaCl_2$, 0.5 mM spermidine, 0.075% NP-40, 1 mM β-Mercaptoethanol) by pipetting till homogeneity and divided into 6x 250 μl aliquots. We added a range of MNase amounts to the aliquots (typically 0, 0.01, 0.02, 0.04, 0.06, and 0.1 U) and rotated the tubes at 37°C for 45 minutes. We terminated the reaction by adding 25 mM EDTA and 0.5% SDS, added 150 μg Proteinase K and incubated at 37°C for one hour to digest proteins and at 65°C overnight to de-crosslink. We performed a phenol/chloroform extraction and ethanol/NaCl precipitation and resuspended in 53 μl TE (10 mM Tris, 1 mM EDTA, pH 8) buffer. We added 10 μg RNAse A and incubated at 37°C for ≥1 h. For each sample aliquot we withdrew 5 μl, mixed with 6x Amaranth loading buffer (15% Ficoll-400, 20 mM Tris-HCl, 60 mM EDTA, 0.1% Amaranth, pH 7.5), and ran on a 2% agarose gel to inspect the MNase digestion pattern. We picked the sample aliquot, where 4-5 bands of the nucleosome ladder were visible and most intensity was in the mononucleosomal band. We performed a SPRI bead cleanup with a 1.8:1 beads:DNA solution ratio using home-made SPRI beads (prepared according to dx.doi.org/10.17504/protocols.io.bnz4mf8w) following instructions for AMPure XP beads (Beckman Coulter). We eluted in CutSmart buffer, added 10 U Quick CIP, incubated for 10 minutes at 37°Cto remove 3’ phosphates, and heat-inactivated at 80°C for 2 minutes. We added 6x Amaranth loading buffer containing 60x SYBR Gold Nucleic Acid Gel Stain (Invitrogen), ran the sample on a 1x TAE 2% LMP agarose gel, and excised the mononucleosomal DNA band on a blue light screen. We performed a β-Agarase I (NEB) digest according to the manufacturer’s instructions, followed by a phenol/chloroform extraction and ethanol/NaCl precipitation. We resuspended in 10 mM Tris pH 7.5 and performed an end-repair using the NEBNext end repair module according to the manufacturer’s instructions followed by a 1.8:1 SPRI bead cleanup. To A-tail, we eluted in NEBuffer 2, added 100 μM dATP and 10 U Klenow fragment 3’-5’ exo^- and incubated at 37°C for 30 minutes, followed by a 1.8:1 SPRI bead cleanup. We eluted in T4 DNA Ligase buffer and ligated with 5 μM universal adapter and 800 U T4 DNA Ligase at 16°C overnight. The universal adapter contained a 3’-T overhang and P5 and P7-specific flaps and was annealed from oRG827 and oRG828 (see Table S3 for sequences) in Annealing Buffer (10 mM Tris-HCl, 50 mM NaCl, 1 mM EDTA, pH 7.5) by heating to 95°C for 5 minutes and slowly cooling to 4°C over the course of 2 hours. We performed a 1:1 SPRI bead cleanup and eluted in 30 µl 10 mM Tris pH 7.5. We used 3x 10 µl eluate in separate PCR amplification reactions with the KAPA HiFi PCR Kit according to the manufacturer's instructions (see Table S3 for library amplification primer sequences). We amplified with 12 cycles, checked for visible products by Ethidium bromide agarose gel electrophoresis, and ran additional PCR cycles if necessary. We performed a 1:1 SPRI bead cleanup. We performed a preparative gel electrophoresis (1x TAE 1.5% LMP agarose) as described above, excised the band corresponding to mononucleosomes (centered at ca. 270 bp, mononucleosomal DNA + adapters), performed a β-Agarase I digest, a phenol/chloroform extraction, and an ethanol/ammonium acetate precipitation. We quantified the DNA concentration with the Qubit Flex system, analyzed the fragment size distribution with a Bioanalyzer High Sensitivity DNA chip, and deep-sequenced pooled libraries using the NextSeq 500 System (Illumina) with 2x75 bp paired reads.

Pho5 assay: We used a colorimetric assay to determine the activity of the cell surface-bound Pho5 enzyme [77]. We collected exponentially growing yeast cells by centrifugation, washed with 100 mM Sodium acetate pH 4.0 (NaAc), and diluted in NaAc to an OD of 1.5 at 600 nm ($2.7 \cdot 10^7$ cells/ml). We mixed 50 µl cell suspension with 200 µl freshly prepared 20 mM p-Nitrophenylphosphate (PNPP) in NaAc, incubated at 30°C for 15 minutes with shaking at 1200 rpm, and stopped the reaction by addition of 250 µl 10% TCA. We alkalized the pH by addition of 500 µl 2 M Na_2CO_3, collected the cells by centrifugation at 21,000 g for 1 minute, and measured the OD of the supernatant at 405 nm. One unit (U) of Pho5 activity A is defined as the amount of enzyme which catalyzes the liberation of 1 nmol PNPP per minute and OD_{600nm} unit under the described assay conditions and was calculated with the formula

$$A = \frac{OD_{405nm}}{\varepsilon \cdot l \cdot t \cdot OD_{600nm}} \cdot f \cdot V$$

where / is the pass length (1 cm), t is the reaction time (15 minutes), f is a conversion factor (10^9 nM/1M), and V is the reaction volume (0.25 ml), ε is the extinction coefficient (4519 $M^{-1} \cdot cm^{-1}$), which we determined for our assay setup using a p-Nitrophenol concentration series. Analysis scripts can be found at https://doi.org/10.5281/zenodo.7508119.

Flow cytometry: We collected ca. $6.5 \cdot 10^6$ cells per sample by centrifugation at 3,000 g and room temperature for 2 minutes. We washed with PBS (137 mM NaCl, 12 mM Phosphate, 2.7 mM KCl, pH 7.4) and fixated the cells in 1.5 ml PBS containing 1% formaldehyde for 30 minutes at room temperature on the nutator. We washed twice with PBS, resuspended in 1.8 ml PBS, and stored at 4°C in the dark. We analyzed fluorescence using a LSRFortessa (Becton Dickinson) and FACSDiva (Becton Dickinson) software. We measured mKate2 fluorescence using a 561 nm laser for excitation, a 600 nm long-pass filter, and a 610/20 nm emission filter. We measured Citrine fluorescence using a 488 nm laser for excitation, a 505 nm long-pass filter, and a 525/50 nm emission filter. We gated for unbudded cells using the SSC and FSC channels. Analysis scripts can be found at https://doi.org/10.5281/zenodo.7508119.

Reverse Transcription (RT)-qPCR: We grew yeast cells as for S1-seq library preparation (including G2/M arrest and Rapamycin treatment) and collected ca. $8 \cdot 10^7$ cells. To extract total RNA, we resuspended cell pellets in 400 µl TES buffer (10 mM Tris pH7.5, 10 mM EDTA pH 8, 0.5% SDS), 400 µl acidic phenol/chloroform, and 50 µl Zirconia/Silica beads. We lysed cells by shaking at 1,400 rpm and 65°C for 30 minutes. After centrifugation at 20,000 g and 4°C for 5 minutes, the aqueous phase was mixed with 1 ml of ethanol and 40 µl 3 M NaAc pH 5.5. After incubation on ice for 30 minutes, the precipitated RNA was collected by centrifugation at 20,000 g and 4°C for 20 minutes, washed with ice-cold 80% ethanol, dried for 1 hour, and resuspended in 80 µl water. Potential genomic DNA contaminations were removed by two rounds of digestion with 20 U Turbo DNase at 37°C for 30 minutes followed by ethanol/NaAc precipitation. The final RNA pellet was resuspended in 50 µl water and quantified by photometry. To confirm the integrity of the extracted RNA, 500 ng of RNA was mixed with RNA Loading Dye, heated to 70°C, chilled on ice for 2 minutes, subjected to electrophoresis on a 1.5% agarose 1x TBE (100 mM Tris-borate, 1 mM EDTA) gel, and stained with 1x SYBR Gold.

Reverse transcription (RT) was performed with the Superscript IV First-Strand Synthesis System using the supplied oligo-dT primer and 5 µg total RNA according to the manufacturer's instructions. Per sample and amplicon, we prepared qPCR triplicates containing 1:100 diluted RT product in 10 mM Tris pH 7.5, 300 nM of each forward and reverse primer (listed in Table S2), and 1x SsoAdvanced Universal SYBR Green Supermix in a total volume of 10 µl and analyzed them on a CFX384 Real-Time System (Biorad) with 10 minutes initial denaturation at 95°C, followed by 40 cycles of 1 minute denaturation at 95°C and 1 minute annealing and extension at 58°C. Transcript levels R relative to the *ADH1* level were calculated according to [70] with the formula

$$R = \frac{E_{target}^{-C_{q\,target}}}{E_{ADH1}^{-C_{q\,ADH1}}}$$

where E_{target} and E_{ADH1} are the primer efficiencies of the target amplicon and the *ADH1* amplicon, respectively, and $C_{q\ target}$ and $C_{q\ ADH1}$ are the quantification cycles for the target and *ADH1* amplicon, respectively. Analysis scripts can be found at https://doi.org/10.5281/zenodo.7508119.

Deep sequencing data analysis: All analysis scripts can be found at https://doi.org/10.5281/zenodo.7508119.

S1-seq libraries that were prepared following protocol version 2 (see Note to the S1-seq library preparation section), contained a constant linker region adjacent to the P7 primer sequence, which resulted in many false N base calls by the bcl2fastq program running with standard parameters. To overcome this, we ran bcl2fastq with parameters --mask-short-adapter-reads 0 --minimum-trimmed-read-length 0 --use-bases-mask Y63N*,I*,Y12N* and a modified SampleSheet.csv file with adapter sequences removed.

Deep-sequencing read mapping and UMI-directed deduplication were achieved with custom BASH scripts using fastp 0.20.1 [78], SAMtools 1.9 [79], Bowtie 2.3.5.1 [80], and UMI-tools

1.0.0 [81] software. To improve read mapping, we employed custom R scripts to modify the reference genome by injecting W303 SNPs reported in [82] and adding relevant strain-specific modifications, such as *HML* and *HMR* deletions, inserted reporter genes, and engineered SrfI cut sites. We then used the bowtie2-build program to derive Bowtie2 indices for read mapping. MNase-seq read mapping was performed with the bowtie parameters --no-mixed --no-discordant. PCR duplicates among MNase-seq reads were removed using the fixmate -m and markdup -r commands from samtools.

Subsequent analyses and data visualizations were performed with custom R scripts using the R libraries GenomicRanges, GenomicAlignments, BSgenome, Biostrings, rmelting, and Gviz [83–85]. High-confidence MRX nick site mapping requires that especially the 5’ read ends fully match the reference genome. To filter out mapped reads where this was not the case, we ran the Bowtie2 mapper with the parameter --local and subsequently discarded alignments with 5’ soft clipping (having “S” as the first letter in their CIGAR string). We also removed non-unique mappings (for which the best and second-best mappings had equal alignment scores). We then calculated S1-seq coverage based on the 5’ alignment ends and normalized to reads per million (RPM) with respect to the nuclear genome; we excluded alignments to the mitochondrial genome from the normalization, as their number continued increasing even after G2/M arrest and DSB induction (data not shown), probably due to cell cycle-decoupled mitochondrial DNA replication.

MNase-seq paired end alignments with a calculated insert size >250 bp were filtered out. In case the insert size distribution had a median value different from the expected 147 bp, we trimmed or expanded all alignments, such that the expected value was reached.

Genomic SrfI recognition sites are cleaved with different kinetics [28]. We grouped DSB sites by cutting kinetics (slow, middle, and fast) based on the summed S1-seq coverage around each SrfI site 1 hour after SrfI induction (Figure S1E). We performed the analysis of average S1-seq coverage spreading for each group separately. Moving average calculations used the runmed function of R, except for the first two nucleotides next to DSBs, where the original values were used, as here the S1-seq signal can be exceptionally high due to unprocessed DSB ends. S1-seq coverage data were smoothed with a Hanning window. MNase-seq data were smoothed with the runmed function of R.

To align nucleosomes and MRX nicking, we identified nucleosome centers by finding local maxima of smoothed (moving mean and spline smoothing) MNase-seq coverage data. We than merged maxima below a minimal distance, removed maxima below a threshold value (to exclude maxima in background noise) and without sufficient MNase-seq coverage decline in the vicinity.

QUANTIFICATION AND STATISTICAL ANALYSIS

Statistical analyses were conducted using the software R (version 4.2.1) and details can be found in the figure legends.

Citations only in SI: [86]

Citations only in KRT: [87]

Supplementary Material

Refer to Web version on PubMed Central for supplementary material.

Acknowledgments

We thank Elena Mimitou for her help with establishing the S1-seq library preparation and Luca Cerato and David Shore for their help with establishing the MNase-seq library preparation. We acknowledge Andreas Hochwagen for his kind gift of anchor-away yeast strains and New England Biolabs for providing the SrfI protein sequence. We thank L. Berchowitz, W.K. Holloman, D.S.M. Ottoz, and members of the Symington laboratory for discussions and comments on the manuscript. This study was supported by grants from the National Institutes of Health (R35 GM126997 and P01 CA174653 to L.S.S.), in part through the NIH/NCI Cancer Center Support Grant P30CA013696 (CCSG DNA Sequencing Core), the Swiss National Science Foundation (31003A_175444 and 310030_205199 to P.C.), and the European Research Council (681630 to P.C.).

References

1. Tubbs A, and Nussenzweig A (2017). Endogenous DNA Damage as a Source of Genomic Instability in Cancer. Cell 168, 644–656. 10.1016/j.cell.2017.01.002. [PubMed: 28187286]
2. Betermier M, Borde V, and de Villartay JP (2020). Coupling DNA Damage and Repair: an Essential Safeguard during Programmed DNA Double-Strand Breaks? Trends Cell Biol 30, 87–96. 10.1016/j.tcb.2019.11.005. [PubMed: 31818700]
3. Moynahan ME, and Jasin M (2010). Mitotic homologous recombination maintains genomic stability and suppresses tumorigenesis. Nat Rev Mol Cell Biol 11, 196–207. 10.1038/nrm2851. [PubMed: 20177395]
4. Taylor AMR, Rothblum-Oviatt C, Ellis NA, Hickson ID, Meyer S, Crawford TO, Smogorzewska A, Pietrucha B, Weemaes C, and Stewart GS (2019). Chromosome instability syndromes. Nat Rev Dis Primers 5, 64. 10.1038/s41572-019-0113-0. [PubMed: 31537806]
5. Chiruvella KK, Liang Z, and Wilson TE (2013). Repair of double-strand breaks by end joining. Cold Spring Harb Perspect Biol 5, a012757. 10.1101/cshperspect.a012757. [PubMed: 23637284]
6. Cejka P, and Symington LS (2021). DNA End Resection: Mechanism and Control. Annu Rev Genet 55, 285–307. 10.1146/annurev-genet-071719-020312. [PubMed: 34813349]
7. Ranjha L, Howard SM, and Cejka P (2018). Main steps in DNA double-strand break repair: an introduction to homologous recombination and related processes. Chromosoma 127, 187–214. 10.1007/s00412-017-0658-1. [PubMed: 29327130]
8. Symington LS, and Gautier J (2011). Double-strand break end resection and repair pathway choice. Annu Rev Genet 45, 247–271. 10.1146/annurev-genet-110410-132435. [PubMed: 21910633]
9. Pham N, Yan Z, Yu Y, Faria Afreen M, Malkova A, Haber JE, and Ira G (2021). Mechanisms restraining break-induced replication at two-ended DNA double-strand breaks. EMBO J 40, e104847. 10.15252/embj.2020104847. [PubMed: 33844333]
10. Cannavo E, and Cejka P (2014). Sae2 promotes dsDNA endonuclease activity within Mre11-Rad50-Xrs2 to resect DNA breaks. Nature 514, 122–125. [PubMed: 25231868]
11. Huertas P, Cortes-Ledesma F, Sartori AA, Aguilera A, and Jackson SP (2008). CDK targets Sae2 to control DNA-end resection and homologous recombination. Nature 455, 689–692. 10.1038/nature07215. [PubMed: 18716619]
12. Ira G, Pellicioli A, Balijja A, Wang X, Fiorani S, Carotenuto W, Liberi G, Bressan D, Wan L, Hollingsworth NM, et al. (2004). DNA end resection, homologous recombination and DNA damage checkpoint activation require CDK1. Nature 431, 1011–1017. 10.1038/nature02964. [PubMed: 15496928]
13. Reginato G, Cannavo E, and Cejka P (2017). Physiological protein blocks direct the Mre11-Rad50-Xrs2 and Sae2 nuclease complex to initiate DNA end resection. Genes & development 31, 2325–2330. [PubMed: 29321179]
14. Wang W, Daley JM, Kwon Y, Krasner DS, and Sung P (2017). Plasticity of the Mre11-Rad50-Xrs2-Sae2 nuclease ensemble in the processing of DNA-bound obstacles. Genes & development 31, 2331–2336. [PubMed: 29321177]

15. Deshpande RA, Myler LR, Soniat MM, Makharashvili N, Lee L, Lees-Miller SP, Finkelstein IJ, and Paull TT (2020). DNA-dependent protein kinase promotes DNA end processing by MRN and CtIP. Sci Adv 6, eaay0922. 10.1126/sciadv.aay0922. [PubMed: 31934630]
16. Garcia V, Phelps SE, Gray S, and Neale MJ (2011). Bidirectional resection of DNA double-strand breaks by Mre11 and Exo1. Nature 479, 241–244. 10.1038/nature10515. [PubMed: 22002605]
17. Mimitou EP, and Symington LS (2008). Sae2, Exo1 and Sgs1 collaborate in DNA double-strand break processing. Nature 455, 770–774. 10.1038/nature07312. [PubMed: 18806779]
18. Zhu Z, Chung WH, Shim EY, Lee SE, and Ira G (2008). Sgs1 helicase and two nucleases Dna2 and Exo1 resect DNA double-strand break ends. Cell 134, 981–994. 10.1016/j.cell.2008.08.037. [PubMed: 18805091]
19. Shibata A, Moiani D, Arvai AS, Perry J, Harding SM, Genois MM, Maity R, van Rossum-Fikkert S, Kertokalio A, Romoli F, et al. (2014). DNA double-strand break repair pathway choice is directed by distinct MRE11 nuclease activities. Mol Cell 53, 7–18. 10.1016/j.molcel.2013.11.003. [PubMed: 24316220]
20. Myler LR, Gallardo IF, Soniat MM, Deshpande RA, Gonzalez XB, Kim Y, Paull TT, and Finkelstein IJ (2017). Single-Molecule Imaging Reveals How Mre11-Rad50-Nbs1 Initiates DNA Break Repair. Mol Cell 67, 891–898 e894. 10.1016/j.molcel.2017.08.002. [PubMed: 28867292]
21. Liu Y, Sung S, Kim Y, Li F, Gwon G, Jo A, Kim AK, Kim T, Song OK, Lee SE, and Cho Y (2016). ATP-dependent DNA binding, unwinding, and resection by the Mre11/Rad50 complex. EMBO J 35, 743–758. 10.15252/embj.201592462. [PubMed: 26717941]
22. Kashammer L, Saathoff JH, Lammens K, Gut F, Bartho J, Alt A, Kessler B, and Hopfner KP (2019). Mechanism of DNA End Sensing and Processing by the Mre11-Rad50 Complex. Mol Cell 76, 382–394 e386. 10.1016/j.molcel.2019.07.035. [PubMed: 31492634]
23. Seifert FU, Lammens K, Stoehr G, Kessler B, and Hopfner KP (2016). Structural mechanism of ATP-dependent DNA binding and DNA end bridging by eukaryotic Rad50. EMBO J 35, 759–772. 10.15252/embj.201592934. [PubMed: 26896444]
24. Cannon B, Kuhnlein J, Yang SH, Cheng A, Schindler D, Stark JM, Russell R, and Paull TT (2013). Visualization of local DNA unwinding by Mre11/Rad50/Nbs1 using single-molecule FRET. Proc Natl Acad Sci U S A 110, 18868–18873. 10.1073/pnas.1309816110. [PubMed: 24191051]
25. Gut F, Kashammer L, Lammens K, Bartho JD, Boggusch AM, van de Logt E, Kessler B, and Hopfner KP (2022). Structural mechanism of endonucleolytic processing of blocked DNA ends and hairpins by Mre11-Rad50. Mol Cell 82, 3513–3522 e3516. 10.1016/j.molcel.2022.07.019. [PubMed: 35987200]
26. Hopfner KP, Karcher A, Craig L, Woo TT, Carney JP, and Tainer JA (2001). Structural biochemistry and interaction architecture of the DNA double-strand break repair Mre11 nuclease and Rad50-ATPase. Cell 105, 473–485. 10.1016/s0092-8674(01)00335-x. [PubMed: 11371344]
27. Mimitou EP, Yamada S, and Keeney S (2017). A global view of meiotic double-strand break end resection. Science 355, 40–45. 10.1126/science.aak9704. [PubMed: 28059759]
28. Gnügge R, and Symington LS (2020). Efficient DNA double-strand break formation at single or multiple defined sites in the Saccharomyces cerevisiae genome. Nucleic Acids Res 48, e115. 10.1093/nar/gkaa833. [PubMed: 33053188]
29. Haruki H, Nishikawa J, and Laemmli UK (2008). The anchor-away technique: rapid, conditional establishment of yeast mutant phenotypes. Mol Cell 31, 925–932. 10.1016/j.molcel.2008.07.020. [PubMed: 18922474]
30. Maekawa K, Yamada S, Sharma R, Chaudhuri J, and Keeney S (2022). Triple-helix potential of the mouse genome. Proc Natl Acad Sci U S A 119, e2203967119. 10.1073/pnas.2203967119. [PubMed: 35503911]
31. Konig J, Zarnack K, Rot G, Curk T, Kayikci M, Zupan B, Turner DJ, Luscombe NM, and Ule J (2010). iCLIP reveals the function of hnRNP particles in splicing at individual nucleotide resolution. Nat Struct Mol Biol 17, 909–915. 10.1038/nsmb.1838. [PubMed: 20601959]
32. Llorente B, and Symington LS (2004). The Mre11 nuclease is not required for 5’ to 3’ resection at multiple HO-induced double-strand breaks. Mol Cell Biol 24, 9682–9694. 10.1128/MCB.24.21.9682-9694.2004. [PubMed: 15485933]

33. Gobbini E, Casari E, Colombo CV, Bonetti D, and Longhese MP (2020). The 9-1-1 Complex Controls Mre11 Nuclease and Checkpoint Activation during Short-Range Resection of DNA Double-Strand Breaks. Cell Rep 33, 108287. 10.1016/j.celrep.2020.108287. [PubMed: 33086066]

34. Chen X, Xu X, Chen Y, Cheung JC, Wang H, Jiang J, de Val N, Fox T, Gellert M, and Yang W (2021). Structure of an activated DNA-PK and its implications for NHEJ. Mol Cell 81, 801–810 e803. 10.1016/j.molcel.2020.12.015. [PubMed: 33385326]

35. Nemoz C, Ropars V, Frit P, Gontier A, Drevet P, Yu J, Guerois R, Pitois A, Comte A, Delteil C, et al. (2018). XLF and APLF bind Ku80 at two remote sites to ensure DNA repair by non-homologous end joining. Nat Struct Mol Biol 25, 971–980. 10.1038/s41594-018-0133-6. [PubMed: 30291363]

36. Walker JR, Corpina RA, and Goldberg J (2001). Structure of the Ku heterodimer bound to DNA and its implications for double-strand break repair. Nature 412, 607–614. 10.1038/35088000. [PubMed: 11493912]

37. Bazzano D, Lomonaco S, and Wilson TE (2021). Mapping yeast mitotic 5' resection at base resolution reveals the sequence and positional dependence of nucleases in vivo. Nucleic Acids Res 49, 12607–12621. 10.1093/nar/gkab597. [PubMed: 34263309]

38. Zhou T, Yang L, Lu Y, Dror I, Dantas Machado AC, Ghane T, Di Felice R, and Rohs R (2013). DNAshape: a method for the high-throughput prediction of DNA structural features on a genomic scale. Nucleic Acids Res 41, W56–62. 10.1093/nar/gkt437. [PubMed: 23703209]

39. Rohs R, Jin X, West SM, Joshi R, Honig B, and Mann RS (2010). Origins of specificity in protein-DNA recognition. Annu Rev Biochem 79, 233–269. 10.1146/annurev-biochem-060408-091030. [PubMed: 20334529]

40. Komeili A, and O'Shea EK (1999). Roles of phosphorylation sites in regulating activity of the transcription factor Pho4. Science 284, 977–980. 10.1126/science.284.5416.977. [PubMed: 10320381]

41. Korber P, and Barbaric S (2014). The yeast PHO5 promoter: from single locus to systems biology of a paradigm for gene regulation through chromatin. Nucleic Acids Res 42, 10888–10902. 10.1093/nar/gku784. [PubMed: 25190457]

42. Karl LA, Peritore M, Galanti L, and Pfander B (2021). DNA Double Strand Break Repair and Its Control by Nucleosome Remodeling. Front Genet 12, 821543. 10.3389/fgene.2021.821543. [PubMed: 35096025]

43. Shim EY, Hong SJ, Oum JH, Yanez Y, Zhang Y, and Lee SE (2007). RSC mobilizes nucleosomes to improve accessibility of repair machinery to the damaged chromatin. Mol Cell Biol 27, 1602–1613. 10.1128/MCB.01956-06. [PubMed: 17178837]

44. Wiest NE, Houghtaling S, Sanchez JC, Tomkinson AE, and Osley MA (2017). The SWI/SNF ATP-dependent nucleosome remodeler promotes resection initiation at a DNA double-strand break in yeast. Nucleic Acids Res 45, 5887–5900. 10.1093/nar/gkx221. [PubMed: 28398510]

45. Chen X, Cui D, Papusha A, Zhang X, Chu CD, Tang J, Chen K, Pan X, and Ira G (2012). The Fun30 nucleosome remodeller promotes resection of DNA double-strand break ends. Nature 489, 576–580. 10.1038/nature11355. [PubMed: 22960743]

46. Gnugnoli M, Casari E, and Longhese MP (2021). The chromatin remodeler Chd1 supports MRX and Exo1 functions in resection of DNA double-strand breaks. PLoS Genet 17, e1009807. 10.1371/journal.pgen.1009807. [PubMed: 34520455]

47. Peritore M, Reusswig KU, Bantele SCS, Straub T, and Pfander B (2021). Strand-specific ChIP-seq at DNA breaks distinguishes ssDNA versus dsDNA binding and refutes single-stranded nucleosomes. Mol Cell 81, 1841–1853 e1844. 10.1016/j.molcel.2021.02.005. [PubMed: 33651987]

48. Gartenberg MR, and Smith JS (2016). The Nuts and Bolts of Transcriptionally Silent Chromatin in Saccharomyces cerevisiae. Genetics 203, 1563–1599. 10.1534/genetics.112.145243. [PubMed: 27516616]

49. Chiolo I, Minoda A, Colmenares SU, Polyzos A, Costes SV, and Karpen GH (2011). Double-strand breaks in heterochromatin move outside of a dynamic HP1a domain to complete recombinational repair. Cell 144, 732–744. 10.1016/j.cell.2011.02.012. [PubMed: 21353298]

50. Kollarovic G, Topping CE, Shaw EP, and Chambers AL (2020). The human HELLS chromatin remodelling protein promotes end resection to facilitate homologous recombination and contributes to DSB repair within heterochromatin. Nucleic Acids Res 48, 1872–1885. 10.1093/nar/gkz1146. [PubMed: 31802118]

51. Maya-Miles D, Andujar E, Perez-Alegre M, Murillo-Pineda M, Barrientos-Moreno M, Cabello-Lobato MJ, Gomez-Marin E, Morillo-Huesca M, and Prado F (2019). Crosstalk between chromatin structure, cohesin activity and transcription. Epigenetics Chromatin 12, 47. 10.1186/s13072-019-0293-6. [PubMed: 31331360]

52. Manfrini N, Clerici M, Wery M, Colombo CV, Descrimes M, Morillon A, d'Adda di Fagagna F, and Longhese MP (2015). Resection is responsible for loss of transcription around a double-strand break in Saccharomyces cerevisiae. Elife 4. 10.7554/eLife.08942.

53. Ma Y, and Lieber MR (2001). DNA length-dependent cooperative interactions in the binding of Ku to DNA. Biochemistry 40, 9638–9646. 10.1021/bi010932v. [PubMed: 11583164]

54. Connelly JC, Kirkham LA, and Leach DR (1998). The SbcCD nuclease of Escherichia coli is a structural maintenance of chromosomes (SMC) family protein that cleaves hairpin DNA. Proc Natl Acad Sci U S A 95, 7969–7974. 10.1073/pnas.95.14.7969. [PubMed: 9653124]

55. Trujillo KM, and Sung P (2001). DNA structure-specific nuclease activities in the Saccharomyces cerevisiae Rad50*Mre11 complex. J Biol Chem 276, 35458–35464. 10.1074/jbc.M105482200. [PubMed: 11454871]

56. Paull TT, and Gellert M (1999). Nbs1 potentiates ATP-driven DNA unwinding and endonuclease cleavage by the Mre11/Rad50 complex. Genes Dev 13, 1276–1288. 10.1101/gad.13.10.1276. [PubMed: 10346816]

57. Williams RS, Moncalian G, Williams JS, Yamada Y, Limbo O, Shin DS, Groocock LM, Cahill D, Hitomi C, Guenther G, et al. (2008). Mre11 dimers coordinate DNA end bridging and nuclease processing in double-strand-break repair. Cell 135, 97–109. 10.1016/j.cell.2008.08.017. [PubMed: 18854158]

58. Kubik S, Bruzzone MJ, Challal D, Dreos R, Mattarocci S, Bucher P, Libri D, and Shore D (2019). Opposing chromatin remodelers control transcription initiation frequency and start site selection. Nat Struct Mol Biol 26, 744–754. 10.1038/s41594-019-0273-3. [PubMed: 31384063]

59. Kubik S, Bruzzone MJ, Jacquet P, Falcone JL, Rougemont J, and Shore D (2015). Nucleosome Stability Distinguishes Two Different Promoter Types at All Protein-Coding Genes in Yeast. Mol Cell 60, 422–434. 10.1016/j.molcel.2015.10.002. [PubMed: 26545077]

60. Aymard F, Bugler B, Schmidt CK, Guillou E, Caron P, Briois S, Iacovoni JS, Daburon V, Miller KM, Jackson SP, and Legube G (2014). Transcriptionally active chromatin recruits homologous recombination at DNA double-strand breaks. Nat Struct Mol Biol 21, 366–374. 10.1038/nsmb.2796. [PubMed: 24658350]

61. Lesage E, Clouaire T, and Legube G (2021). Repair of DNA double-strand breaks in RNAPI- and RNAPII-transcribed loci. DNA Repair (Amst) 104, 103139. 10.1016/j.dnarep.2021.103139. [PubMed: 34111758]

62. Chang EY, Tsai S, Aristizabal MJ, Wells JP, Coulombe Y, Busatto FF, Chan YA, Kumar A, Dan Zhu Y, Wang AY, et al. (2019). MRE11-RAD50-NBS1 promotes Fanconi Anemia R-loop suppression at transcription-replication conflicts. Nat Commun 10, 4265. 10.1038/s41467-019-12271-w. [PubMed: 31537797]

63. Cannavo E, Reginato G, and Cejka P (2019). Stepwise 5' DNA end-specific resection of DNA breaks by the Mre11-Rad50-Xrs2 and Sae2 nuclease ensemble. Proceedings of the National Academy of Sciences of the United States of America 116, 5505–5513. [PubMed: 30819891]

64. Kissling VM, Reginato G, Bianco E, Kasaciunaite K, Tilma J, Cereghetti G, Schindler N, Lee SS, Guerois R, Luke B, et al. (2022). Mre11-Rad50 oligomerization promotes DNA double-strand break repair. Nat Commun 13, 2374. 10.1038/s41467-022-29841-0. [PubMed: 35501303]

65. Donze D, Adams CR, Rine J, and Kamakaka RT (1999). The boundaries of the silenced HMR domain in Saccharomyces cerevisiae. Genes Dev 13, 698–708. 10.1101/gad.13.6.698. [PubMed: 10090726]

66. Thurtle DM, and Rine J (2014). The molecular topography of silenced chromatin in Saccharomyces cerevisiae. Genes Dev 28, 245–258. 10.1101/gad.230532.113. [PubMed: 24493645]
67. Gnügge R, Liphardt T, and Rudolf F (2016). A shuttle vector series for precise genetic engineering of Saccharomyces cerevisiae. Yeast 33, 83–98. 10.1002/yea.3144. [PubMed: 26647923]
68. Ryan OW, Skerker JM, Maurer MJ, Li X, Tsai JC, Poddar S, Lee ME, DeLoache W, Dueber JE, Arkin AP, and Cate JH (2014). Selection of chromosomal DNA libraries using a multiplex CRISPR system. Elife 3. 10.7554/eLife.03703.
69. Gnügge R, Oh J, and Symington LS (2018). Processing of DNA Double-Strand Breaks in Yeast. Methods Enzymol 600, 1–24. 10.1016/bs.mie.2017.11.007. [PubMed: 29458754]
70. Pfaffl MW (2001). A new mathematical model for relative quantification in real-time RT-PCR. Nucleic Acids Res 29, e45. 10.1093/nar/29.9.e45. [PubMed: 11328886]
71. Zierhut C, and Diffley JF (2008). Break dosage, cell cycle stage and DNA replication influence DNA double strand break response. EMBO J 27, 1875–1885. 10.1038/emboj.2008.111. [PubMed: 18511906]
72. Mimitou EP, and Keeney S (2018). S1-seq Assay for Mapping Processed DNA Ends. Methods Enzymol 601, 309–330. 10.1016/bs.mie.2017.11.031. [PubMed: 29523237]
73. Pinto C, Anand R, and Cejka P (2018). Methods to Study DNA End Resection II: Biochemical Reconstitution Assays. Methods Enzymol 600, 67–106. 10.1016/bs.mie.2017.11.009. [PubMed: 29458776]
74. Oh J, Al-Zain A, Cannavo E, Cejka P, and Symington LS (2016). Xrs2 Dependent and Independent Functions of the Mre11-Rad50 Complex. Mol Cell 64, 405–415. 10.1016/j.molcel.2016.09.011. [PubMed: 27746018]
75. Cannavo E, Johnson D, Andres SN, Kissling VM, Reinert JK, Garcia V, Erie DA, Hess D, Thoma NH, Enchev RI, et al. (2018). Regulatory control of DNA end resection by Sae2 phosphorylation. Nat Commun 9, 4016. 10.1038/s41467-018-06417-5. [PubMed: 30275497]
76. Cole HA, Howard BH, and Clark DJ (2012). Genome-wide mapping of nucleosomes in yeast using paired-end sequencing. Methods Enzymol 513, 145–168. 10.1016/B978-0-12-391938-0.00006-9. [PubMed: 22929768]
77. To EA, Ueda Y, Kakimoto SI, and Oshima Y (1973). Isolation and characterization of acid phosphatase mutants in Saccharomyces cerevisiae. J Bacteriol 113, 727–738. 10.1128/jb.113.2.727-738.1973. [PubMed: 4570606]
78. Chen S, Zhou Y, Chen Y, and Gu J (2018). fastp: an ultra-fast all-in-one FASTQ preprocessor. Bioinformatics 34, i884–i890. 10.1093/bioinformatics/bty560. [PubMed: 30423086]
79. Li H, Handsaker B, Wysoker A, Fennell T, Ruan J, Homer N, Marth G, Abecasis G, Durbin R, and Genome Project Data Processing, S. (2009). The Sequence Alignment/Map format and SAMtools. Bioinformatics 25, 2078–2079. 10.1093/bioinformatics/btp352. [PubMed: 19505943]
80. Langmead B, and Salzberg SL (2012). Fast gapped-read alignment with Bowtie 2. Nat Methods 9, 357–359. 10.1038/nmeth.1923. [PubMed: 22388286]
81. Smith T, Heger A, and Sudbery I (2017). UMI-tools: modeling sequencing errors in Unique Molecular Identifiers to improve quantification accuracy. Genome Res 27, 491–499. 10.1101/gr.209601.116. [PubMed: 28100584]
82. Matheson K, Parsons L, and Gammie A (2017). Whole-Genome Sequence and Variant Analysis of W303, a Widely-Used Strain of Saccharomyces cerevisiae. G3 (Bethesda) 7, 2219–2226. 10.1534/g3.117.040022. [PubMed: 28584079]
83. Lawrence M, Huber W, Pages H, Aboyoun P, Carlson M, Gentleman R, Morgan MT, and Carey VJ (2013). Software for computing and annotating genomic ranges. PLoS Comput Biol 9, e1003118. 10.1371/journal.pcbi.1003118. [PubMed: 23950696]
84. Lawrence M, Gentleman R, and Carey V (2009). rtracklayer: an R package for interfacing with genome browsers. Bioinformatics 25, 1841–1842. 10.1093/bioinformatics/btp328. [PubMed: 19468054]
85. Hahne F, and Ivanek R (2016). Visualizing Genomic Data Using Gviz and Bioconductor. Methods Mol Biol 1418, 335–351. 10.1007/978-1-4939-3578-9_16. [PubMed: 27008022]

86. Acar M, Becskei A, and van Oudenaarden A (2005). Enhancement of cellular memory by reducing stochastic transitions. Nature 435, 228–232. 10.1038/nature03524. [PubMed: 15889097]

87. Bhaskara V, Dupre A, Lengsfeld B, Hopkins BB, Chan A, Lee JH, Zhang X, Gautier J, Zakian V, and Paull TT (2007). Rad50 adenylate kinase activity regulates DNA tethering by Mre11/Rad50 complexes. Mol Cell 25, 647–661. 10.1016/j.molcel.2007.01.028. [PubMed: 17349953]

Highlights

- MRX preferentially cleaves 5’ to C within a AT-rich sequence
- MRX nicking spreads over time suggesting repetitive cycles of cleavage
- Ku guides the location of MRX nicks close to DSBs
- MRX nicking is mildly impeded by nucleosome occupancy and transcription

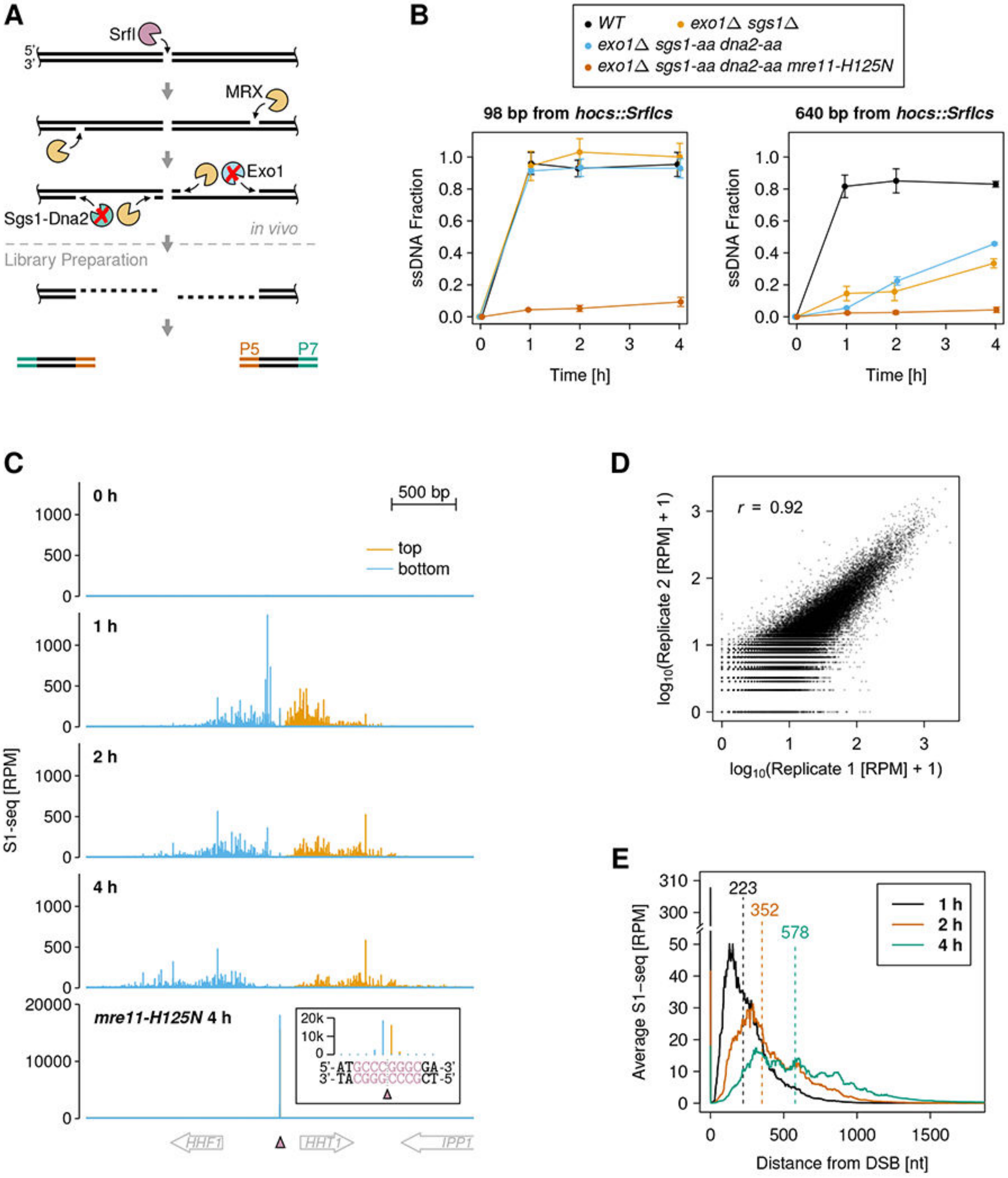

Figure 1. Monitoring Mre11-Rad50-Xrs2 (MRX) nicking at nucleotide resolution

(A) Schematic representation of DSB end resection and the MRX nick site mapping approach. SrfI expression creates multiple defined DSBs and long-range resection suppression preserves MRX nick sites as single-stranded/double-stranded DNA junctions. S1-seq libraries are prepared by *in vitro* blunting and adapter (P5 and P7) ligation and allow nucleotide (nt)-resolution MRX nick site mapping.

(B) Short-range resection (left panel) and long-range resection (right panel) were monitored at the indicated distances from a DSB formed at *hocs::SrfIcs*, where an SrfI cut site (*SrfIcs*) was engineered into the MATa HO cut site (*HOcs*). Data are represented as mean ± standard deviation (SD) of three biological replicates.

(C) S1-seq coverage around the SrfI cut site at chrII:256,173 (pink triangle) at the indicated time points after SrfI induction. The inset shows a zoom-in on the DSB site for the *mre11-H125N exo1*Δ *dna2-aa sgs1-aa* strain. The SrfI recognition sequence is printed in pink and the dotted gray line indicates the blunt cut position. RPM: reads per million reads.

(D) Reproducibility of MRX nick site mapping. S1-seq scores at each nucleotide position in ±2 kbp regions around all DSBs are plotted for two biological replicates (merged 1, 2, and 4 h time points). The Pearson's correlation coefficient *r* is specified.

(E) Average 51-nt smoothed S1-seq coverage spreading from the 9 most efficiently formed DSBs at the indicated time points. Numbers above vertical dashed lines indicate average spreading distance from DSBs. See Figure S1E–G for S1-seq coverage spreading from DSBs with middle and slow formation kinetics.

See also Figures S1 and S2.

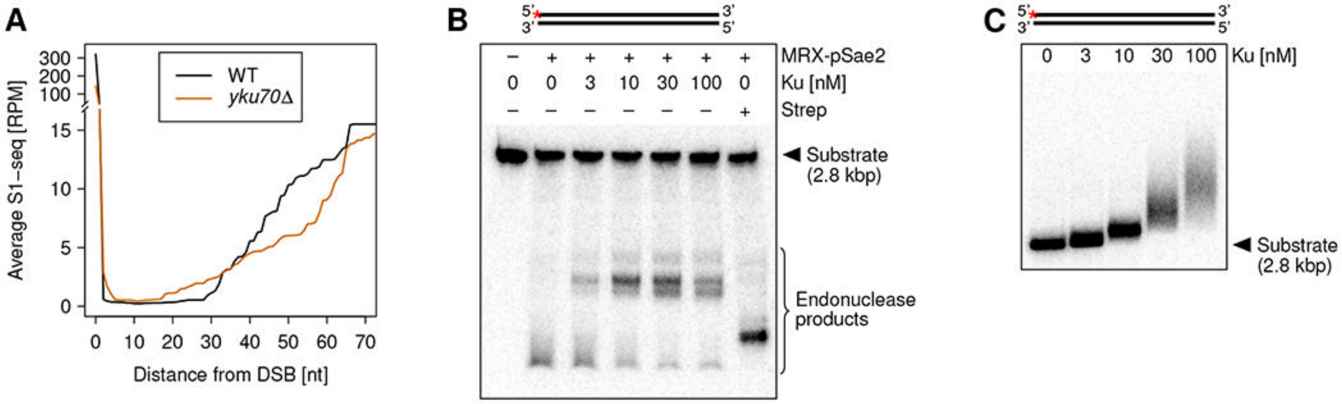

Figure 2. The Ku complex guides DSB-proximal MRX nicks

(A) Average 51-nt smoothed S1-seq coverage near all DSBs 1 h after DSB induction in indicated strains.

(B) *In vitro* MRX nicking in the presence of various concentrations of the yeast Ku complex. The substrate structure is shown on top, and the red asterisk indicates the position of the radioactive label. Ku: Yku70/80 complex. Strep: monovalent Streptavidin (positive control, binding to Biotin residues present at all DNA ends).

(C) Electrophoretic mobility shift assay (EMSA) with Yku70/80 complex (Ku) and 5’ labeled plasmid-length substrate.

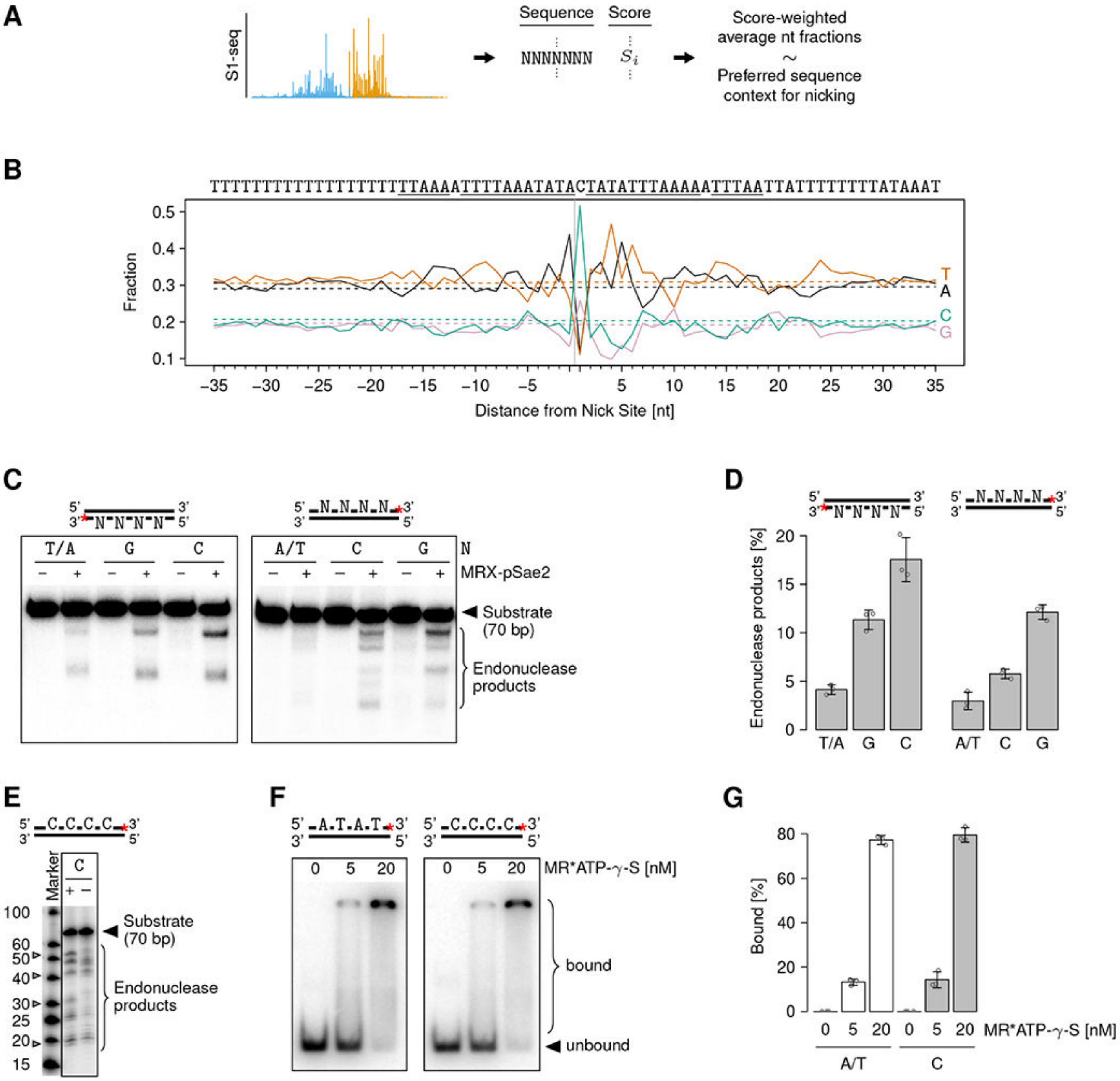

Figure 3. MRX preferentially nicks at a specific sequence motif

(A) Schematic of the analysis approach to identify a potential sequence preference of MRX nicking.

(B) Nucleotide fractions at indicated distances from the MRX nick site (vertical gray line). Color-coded solid and dashed lines show nicking preference (average weighted with S1-seq scores) and background (unweighted average), respectively. The background fractions correspond to the *S. cerevisiae* genome GC content of ca. 38%, as expected. On top, the sequence of the most abundant nucleotide at each position is specified. The rotationally symmetric part of the sequence is underlined.

(C) *In vitro* MRX nicking assay with substrates containing or lacking positioned Cs or Gs.

(D) Quantification of nicking assays such as shown in (C). Individual values (circles) and means (bar heights) ± SD (error bars) of three independent replicates are shown.

(E) Nicking products of the indicated substrates resolved on a higher-resolution gel. The gray filled triangles mark the expected product sizes for MRX nicking at the positioned Cs.

(F) EMSA with ATP-γ-S-bound Mre11-Rad50 (MR) complex and substrates containing or lacking Cs.

(G) Quantification of EMSAs such as shown in (F). Individual values (circles) and means (bar heights) ± SD (error bars) of three independent replicates are shown.

(C-F) The substrate structures are shown on top, and the red asterisks indicate the position of the radioactive label.

See also Figure S3.

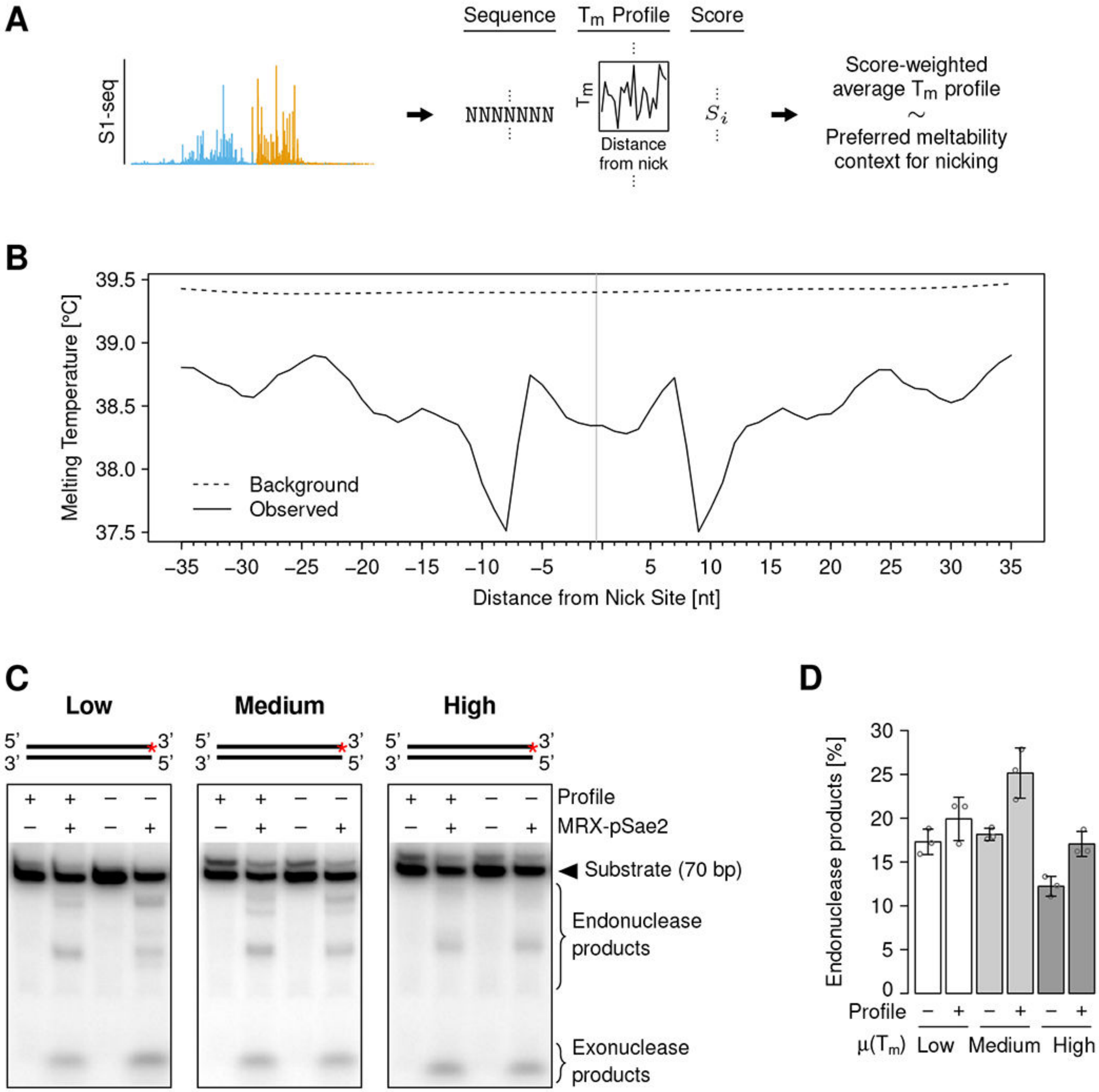

Figure 4. MRX preferentially nicks DNA with a specific melting temperature profile

(A) Schematic of the analysis approach to identify a potential DNA melting profile preference of MRX nicking. T_m: melting temperature.

(B) Melting temperature at indicated distances from the MRX nick site (vertical gray line). Solid and dashed black lines show nicking preference (average weighted with S1-seq score) and background (unweighted average), respectively. Melting temperatures were calculated for 15-bp windows centered at the indicated distance.

(C) *In vitro* MRX nicking of DNA substrates containing or lacking the preferred melting temperature profile and low, medium, or high overall melting temperature, as indicated.

The substrate structures are shown on top, and the red asterisks indicate the position of the radioactive label.

(D) Quantification of nicking assays such as shown in (C). Individual values (circles) and means (bar heights) ± SD (error bars) of three independent replicates are shown. $\mu(T_m)$: average melting temperature.

See also Figure S4.

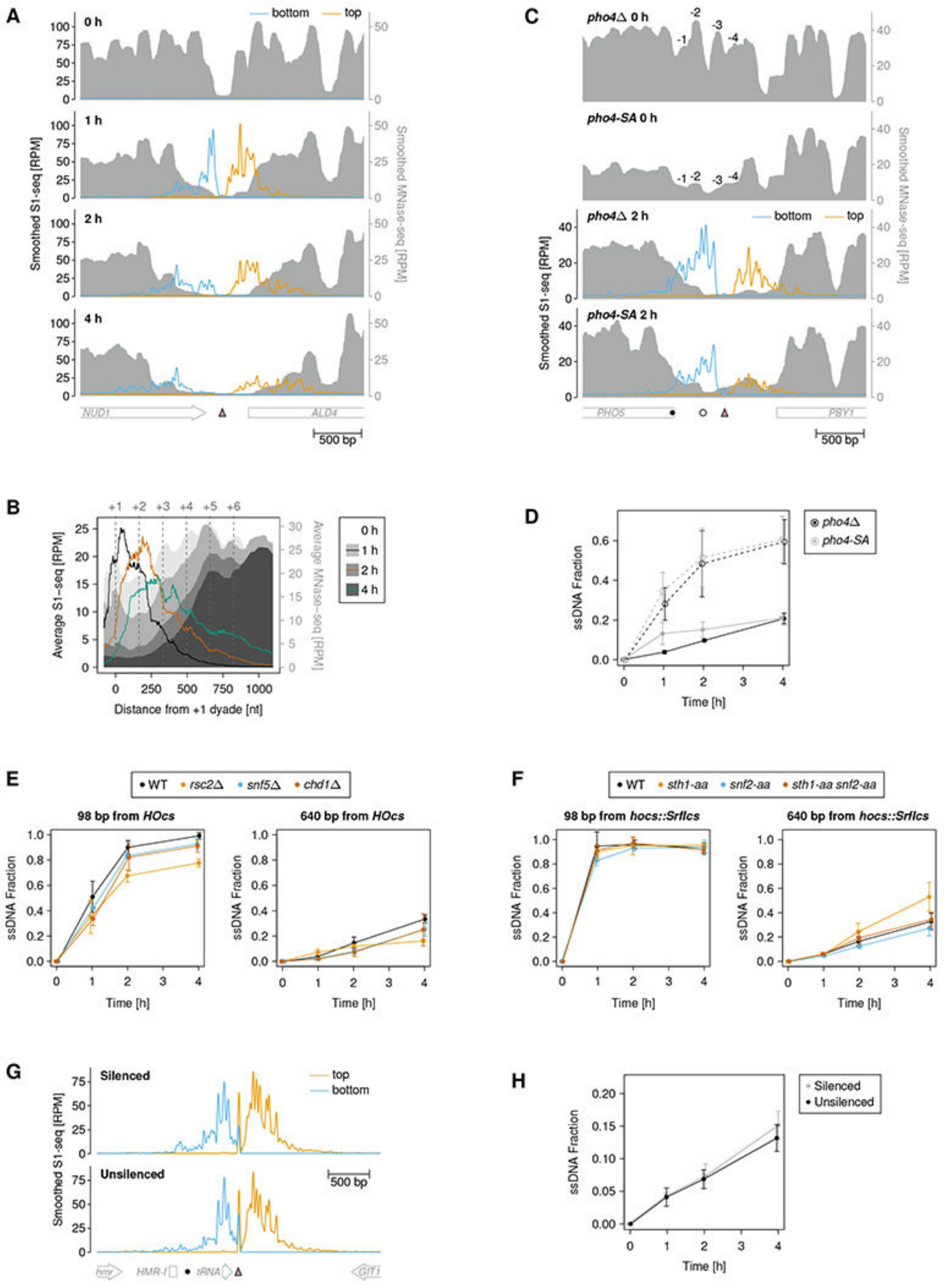

Figure 5. MRX nicking is influenced by nucleosomes, but not by chromatin remodelers or heterochromatin

(A) 51-nt smoothed S1-seq and 31-nt smoothed MNase-seq coverage around the SrfI cut site (pink triangle) at chrXV:1039563 at the indicated time points after SrfI induction.

(B) Average 51-nt smoothed S1-seq and MNase-seq coverage around all DSBs aligned at the first (0 h and 1 h time points), second (2 h time point), or third (4 h time point) nucleosome from the DSB site.

(C) 51-nt smoothed S1-seq and 31-nt smoothed MNase-seq coverage around the SrfI cut site (pink triangle) inserted at the *PHO5* promoter at the indicated time points after DSB induction. The −1 to −4 nucleosomes, which are positioned in the *pho4*Δ strain and depleted in the *pho4-SA* strain, are indicated. The filled and empty circle indicate the sites where resection was evaluated using a qPCR-based assay, as shown in (D).

(D) Resection was evaluated at −223 bp (empty circles) and −538 bp (filled circles) from the DSB, as also indicated in (C). Data are represented as mean ± SD of three biological replicates.

(E) Resection was evaluated at the indicated distances from a DSB generated at the *MAT*a HO cut site (*HOcs*) in long-range resection suppressed strains. Data are represented as mean ± SD of three biological replicates.

(F) Resection was evaluated at the indicated distances from a DSB generated at an SrfI cut site engineered into the *MAT*a HO cut site (*hocs::SrfIcs*) in long-range resection suppressed strains. Data are represented as mean ± SD of three biological replicates.

(G) 51-nt smoothed S1-seq coverage around the HO cut site (pink triangle) inserted downstream of the *HMR* locus 2 h after HO induction. In the unsilenced strain, the silencer seed sequence (*HMR-I*) was substituted with an unrelated sequence (*hisG*). Silencing has been reported to spread until the tRNA gene (systematic name: *YNCC0014W*), which serves as a boundary element [65,66]. The filled circle indicates the site where resection was evaluated using a qPCR-based assay, as shown in (H).

(H) Resection was evaluated at −607 bp from the DSB, as also indicated in (G). Data are represented as mean ± SD of three biological replicates.

See also Figure S5.

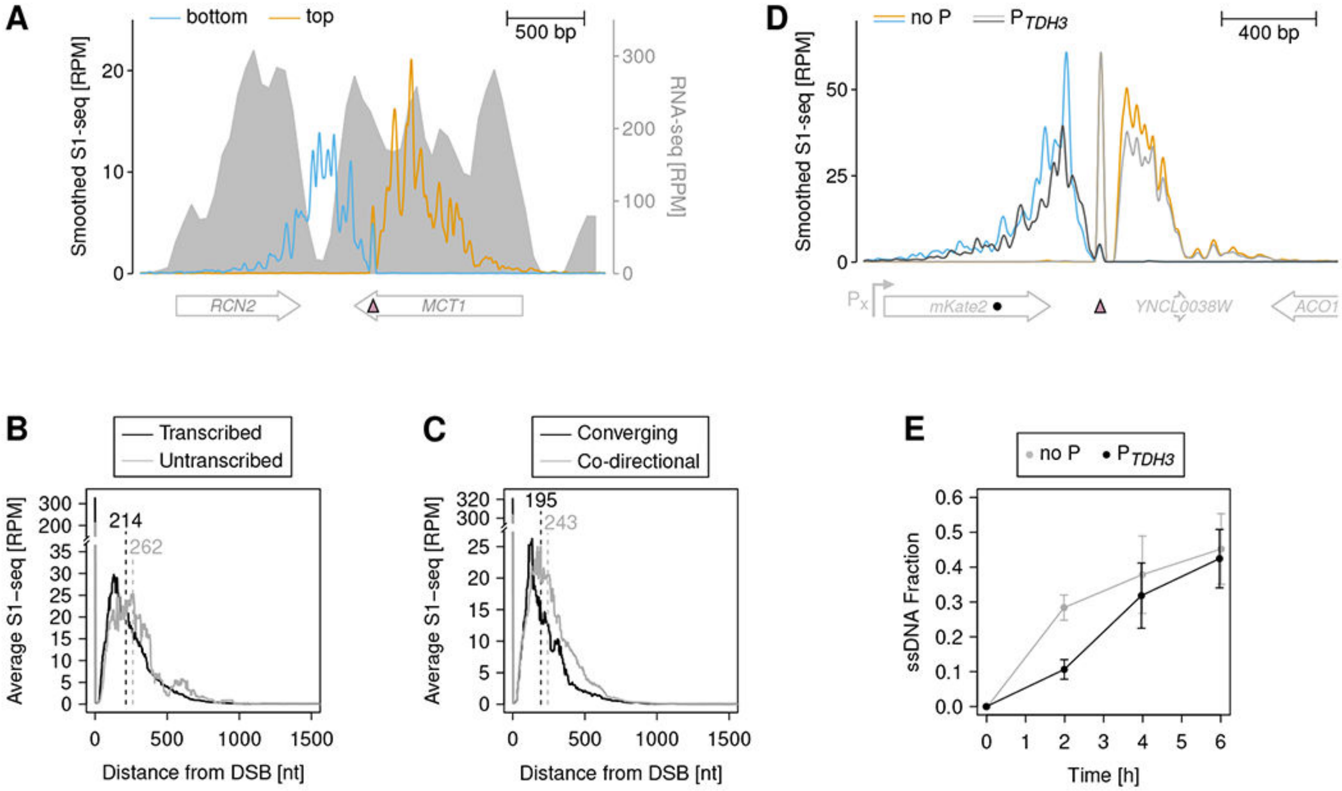

Figure 6. Transcription mildly impedes MRX nicking.

RNA-seq and 51-nt smoothed S1-seq coverage 2 h post DSB induction around the SrfI cut site (pink filled triangle) at chrXV:756594. Note the dip of S1-seq coverage on the bottom strand upon encountering a highly transcribed region.

(B) Average 51-nt smoothed S1-seq coverage spreading from all DSBs 1 h post DSB induction grouped by transcriptional activity. Numbers above vertical dashed lines indicate average spreading distance from DSBs.

(C) Average 51-nt smoothed S1-seq coverage spreading from all DSBs 1 h post DSB induction in transcribed regions grouped by converging or co-directional orientation of transcription and resection. Numbers above vertical dashed lines indicate average spreading distance from DSBs.

(D) 51-nt smoothed S1-seq coverage 2 h post DSB induction around the HO cut site (pink filled triangle) located downstream of the *mKate2* reporter gene. The filled circle indicates the site where resection was evaluated using a qPCR-based assay, as shown in (E). no P: no promoter.

(E) Resection was evaluated at −430 bp from the DSB, as also indicated in (D). Data are represented as mean ± SD of three biological replicates. no P: no promoter.

See also Figure S6.

Key resources table

REAGENT or RESOURCE	**SOURCE**	**IDENTIFIER**
Chemicals, peptides, and recombinant proteins		
Nocodazole	AbMole	Cat# M3194
Rapamycin	Sigma	Cat# 553210
β-Estradiol	Sigma	Cat# E8875
rCutSmart Buffer	New England BioLabs	Cat# B6004S
RsaI	New England BioLabs	Cat# R0167S
AluI	New England BioLabs	Cat# R0137S
StyI-HF	New England BioLabs	Cat# R3500S
MseI	New England BioLabs	Cat# R0525S
Certified Low Melt Agarose	Bio-Rad	Cat# 1613111
S1 Nuclease	Promega	Cat# M5761
dNTP Mix	Promega	Cat# U1515
T4 DNA Polymerase	New England BioLabs	Cat# M0203L
dATP Solution	New England BioLabs	Cat# N0440S
Klenow Fragment (3’-5’ exo$^-$)	New England BioLabs	Cat# M0212S
T4 DNA Ligase	New England BioLabs	Cat# M0202L
β-Agarase I	New England BioLabs	Cat# M0392S
UltraPure Phenol:Chloroform:Isoamyl Alcohol (25:24:1, v/v)	Invitrogen	Cat# 15593-031
6x Gel loading dye without SDS	New England BioLabs	Cat# B7025S
SYBR Gold Nucleic Acid Gel Stain	Invitrogen	Cat# S11494
Formaldehyde	Fisher	Cat# F79-1
Zymolyase 100T	US Biological	Cat# Z1004
Nonidet P-40 substitute	Sigma	Cat# 11754599001
Spermidine	Sigma	Cat# 85558
MNase	Sigma	Cat# N5386
RNAse A	Lucigen	Cat# MRNA092
Ficoll-400	Sigma	Cat# F4375
Amaranth	Sigma	Cat# A1016
Quick CIP	New England BioLabs	Cat# M0525S
p-Nitrophenylphosphate	Sigma	Cat# 4876
p-Nitrophenol	Sigma	Cat# 241326
Acid-Phenol:Chloroform, pH 4.5 (with IAA, 125:24:1)	Invitrogen	Cat# AM9720
Turbo DNase	Invitrogen	Cat# AM2238
RNA Loading Dye	New England BioLabs	Cat# B0363S
Terminal Deoxynucleotidyl Transferase	New England BioLabs	Cat# M0315S
[α-32P]dCTP	PerkinElmer	Cat# BLU013H500UC

REAGENT or RESOURCE	**SOURCE**	**IDENTIFIER**
T4 polynucleotide kinase	New England BioLabs	Cat# M0201S
[γ-32P]ATP	PerkinElmer	Cat# BLU502A500UC
Pyruvate Kinase from rabbit muscle	Sigma	Cat# P1506-5KU
Proteinase K, recombinant, PCR Grade	Sigma	Cat# 000000003115828001
Critical commercial assays		
MasterPure Yeast DNA Purification Kit	Biosearch Technologies	Cat# MPY80200
SsoAdvanced Universal SYBR Green Supermix	Bio-Rad	Cat# 1725274
NEBNext end repair module	New England BioLabs	Cat# E6050S
KAPA HiFi PCR Kit	Roche	Cat# 07958838001
Qubit 1X dsDNA High Sensitivity Assay Kit	Invitrogen	Cat# Q33231
High Sensitivity DNA Kit	Agilent	Cat# 5067-4626
NextSeq 500/550 Mid Output Kit v2.5 (150 Cycles)	Illumina	Cat# 20024904
NextSeq PhiX Control Kit	Illumina	Cat# FC-110-3002
SuperScript IV First-Strand Synthesis System	Invitrogen	Cat# 18091050
Deposited data		
S1-seq and MNase-seq data	This paper	SRA: PRJNA821913
Analysis code	This paper	https://doi.org/10.5281/zenodo.7508119
Original gel image files	This paper	https://doi.org/10.5281/zenodo.7508157
Experimental models: Cell lines		
ExpiSf9™ Cells	Life Technologies	Cat# A35243
Experimental models: Organisms/strains		
Saccharomyces cerevisiae W303: LSY4376-3C: *MAT*a *fpr1::natMX RPL13A-2xFKBP12::TRP1 tor1-1::HIS3 RAD5 hml::pRS-1 hmr::pRS-2 hocs::SrfIcs leu2::*P_{lexO_4}*-SrfI-*T_{CYC1}*-*P_{ACT1}*-LexA-ER-B112-*T_{CYC1}*-LEU2MX rad51::URA3MX*	This paper	N/A
Saccharomyces cerevisiae W303: LSY4376-4A: *MAT*a *fpr1::natMX RPL13A-2xFKBP12::TRP1 tor1-1::HIS3 RAD5 hml::pRS-1 hmr::pRS-2 hocs::SrfIcs leu2::*P_{lexO_4}*-SrfI-*T_{CYC1}*-*P_{ACT1}*-LexA-ER-B112-*T_{CYC1}*-LEU2MX exo1::kanMX sgs1::hphMX rad51::URA3MX*	This paper	N/A
Saccharomyces cerevisiae W303: LSY4377-12B: *MAT*a *RAD5 hml::pRS-1 hmr::pRS-2 fpr1::natMX RPL13A-2xFKBP12::TRP1 tor1-1::HIS3 sgs1-frb-hphMX dna2-frb-hphMX hocs::SrfIcs leu2::*P_{lexO_4}*-SrfI-*T_{CYC1}*-*P_{ACT1}*-LexA-ER-B112-*T_{CYC1}*-LEU2MX exo1::kanMX rad51::URA3MX*	This paper	N/A
Saccharomyces cerevisiae W303: LSY4377-15A: *MAT*a *RAD5 hml::pRS-1 hmr::pRS-2 fpr1::natMX RPL13A-2xFKBP12::TRP1 tor1-1::HIS3 sgs1-frb-hphMX dna2-frb-hphMX hocs::SrfIcs leu2::*P_{lexO_4}*-SrfI-*T_{CYC1}*-*P_{ACT1}*-LexA-ER-B112-*T_{CYC1}*-LEU2MX exo1::kanMX mre11-H125N rad51::URA3MX*	This paper	N/A
Saccharomyces cerevisiae W303: LSY4518-13B: *MAT*a *RAD5 hml::pRS-1 hmr::pRS-2 fpr1Δ RPL13A-2xFKBP12::TRP1 tor1-1 sgs1-frb-hphMX dna2-*	This paper	N/A

REAGENT or RESOURCE	SOURCE	IDENTIFIER
frb-hphMX hocs::SrfIcs leu2::P_{lexO_4}-SrfI-T_{CYC1}-P_{ACT1}-LexA-ER-B112-T_{CYC1}-LEU2MX exo1::kanMX rad51::URA3MX met15Δ		
Saccharomyces cerevisiae W303: LSY4602-20C: MATa RAD5 hml::pRS-1 hmr::pRS-2 fpr1Δ RPL13A-2xFKBP12::TRP1 tor1-1 sgs1-frb-hphMX dna2-frb-hphMX hocs::SrfIcs leu2::P_{lexO_4}-SrfI-T_{CYC1}-P_{ACT1}-LexA-ER-B112-T_{CYC1}-LEU2MX exo1::kanMX rad51::URA3MX met15Δ ku70::altNatMX	This paper	N/A
Saccharomyces cerevisiae W303: LSY4741-8C: MATa RAD5 hml::pRS-1 hmr::pRS-2 fpr1Δ RPL13A-2xFKBP12::TRP1 tor1-1 sgs1-frb-hphMX dna2-frb-hphMX exo1::kanMX rad51::URA3MX met15Δ leu2::P_{lexO_4}-HO-T_{CYC1}-P_{ACT1}-LexA-ER-B112-T_{CYC1}-LEU2MX	This paper	N/A
Saccharomyces cerevisiae W303: LSY4753-3B: MATa RAD5 hml::pRS-1 fpr1Δ RPL13A-2xFKBP12::TRP1 tor1-1 sgs1-frb-hphMX dna2-frb-hphMX exo1::kanMX rad51::URA3MX met15Δ leu2::P_{lexO_4}-HO-T_{CYC1}-P_{ACT1}-LexA-ER-B112-T_{CYC1}-LEU2MX hmr::P_{GAL1}-Citrine-T_{CYC1}-YCRWdelta13::hisG-HOcs@chr3:295659	This paper	N/A
Saccharomyces cerevisiae W303: LSY4754-3A: MATa RAD5 hml::pRS-1 fpr1Δ RPL13A-2xFKBP12::TRP1 tor1-1 sgs1-frb-hphMX dna2-frb-hphMX exo1::kanMX rad51::URA3MX met15Δ leu2::P_{lexO_4}-HO-T_{CYC1}-P_{ACT1}-LexA-ER-B112-T_{CYC1}-LEU2MX hmr::hmr-e::hisG-P_{GAL1}-Citrine-T_{CYC1}-YCRWdelta13::hisG-hmr-i::hisG-HOcs@chr3:295659	This paper	N/A
Saccharomyces cerevisiae W303: LSY4810-41D: MATa RAD5 hml::pRS-1 hmr::pRS-2 fpr1Δ RPL13A-2xFKBP12::TRP1 tor1-1 sgs1-frb-hphMX dna2-frb-hphMX leu2::P_{lexO_4}-HO-T_{CYC1}-P_{ACT1}-LexA-ER-B112-T_{CYC1}-LEU2MX his3::Citrine-HOcs-HA-T_{CYC1}-HIS3MX met15Δ::P_{TDH3}-mKate2-T_{CYC2}-HOcs-MET15 exo1::kanMX rad51::URA3MX	This paper	N/A
Saccharomyces cerevisiae W303: LSY4811-11B: MATa RAD5 hml::pRS-1 hmr::pRS-2 fpr1Δ RPL13A-2xFKBP12::TRP1 tor1-1 sgs1-frb-hphMX dna2-frb-hphMX leu2::P_{lexO_4}-HO-T_{CYC1}-P_{ACT1}-LexA-ER-B112-T_{CYC1}-LEU2MX his3::P_{TDH3}-Citrine-hisG-HOcs-HA-T_{CYC1}-HIS3MX met15Δ::P_{ACT1}-mKate2-T_{CYC2}-HOcs-MET15 exo1::kanMX rad51::URA3MX	This paper	N/A
Saccharomyces cerevisiae W303: LSY4812-5A: MATa RAD5 hml::pRS-1 hmr::pRS-2 fpr1Δ RPL13A-2xFKBP12::TRP1 tor1-1 sgs1-frb-hphMX dna2-frb-hphMX leu2::P_{lexO_4}-HO-T_{CYC1}-P_{ACT1}-LexA-ER-B112-T_{CYC1}-LEU2MX his3::P_{ACT1}-Citrine-hisG-HOcs-HA-T_{CYC1}-HIS3MX met15Δ::mKate2-T_{CYC2}-HOcs-MET15 exo1::kanMX rad51::URA3MX	This paper	N/A
Saccharomyces cerevisiae W303: LSY4815-25B: MATa RAD5 hml::pRS-1 hmr::pRS-2 fpr1Δ RPL13A-2xFKBP12::TRP1 tor1-1 sgs1-frb-hphMX dna2-frb-hphMX met15Δ leu2::P_{lexO_4}-HO-T_{CYC1}-P_{ACT1}-LexA-ER-B112-T_{CYC1}-LEU2MX his3::P_{lexO_4}-SrfI-T_{CYC1}-P_{ACT1}-LexA-ER-B112-T_{CYC1}-HIS3MX exo1::kanMX rad51::URA3MX	This paper	N/A
Saccharomyces cerevisiae W303: LSY4822-3C: MATa RAD5 hml::pRS-1 hmr::pRS-2 fpr1Δ RPL13A-2xFKBP12::TRP1 tor1-1 sgs1-frb-hphMX dna2-frb-hphMX hocs::SrfIcs leu2::P_{lexO_4}-SrfI-T_{CYC1}-P_{ACT1}-LexA-ER-B112-T_{CYC1}-LEU2MX exo1::kanMX rad51::URA3MX met15Δ sth1-frb-natMX	This paper	N/A
Saccharomyces cerevisiae W303: LSY4994-45D: MATa RAD5 hml::pRS-1 hmr::pRS-2 fpr1Δ RPL13A-2xFKBP12::TRP1 tor1-1 sgs1-frb-hphMX dna2-frb-hphMX hocs::SrfIcs leu2::P_{lexO_4}-SrfI-T_{CYC1}-P_{ACT1}-LexA-ER-B112-T_{CYC1}-LEU2MX exo1::kanMX rad51::URA3MX met15Δ sth1-frb-natMX snf2-frb-HIS3MX	This paper	N/A
Saccharomyces cerevisiae W303: LSY4994-89A: MATa RAD5 hml::pRS-1 hmr::pRS-2 fpr1Δ RPL13A-2xFKBP12::TRP1 tor1-1 sgs1-frb-hphMX dna2-frb-hphMX hocs::SrfIcs leu2::P_{lexO_4}-SrfI-T_{CYC1}-P_{ACT1}-LexA-ER-B112-T_{CYC1}-LEU2MX exo1::kanMX rad51::URA3MX met15Δ snf2-frb-HIS3MX	This paper	N/A
Saccharomyces cerevisiae W303: LSY5023-98C: MATa hocs::SrfIcs RAD5 hml::pRS-1 hmr::pRS-2 fpr1Δ RPL13A-2xFKBP12::TRP1 tor1-1 sgs1-frb-hphMX dna2-frb-hphMX met15Δ pho4::pho4-SA1234PA6 P_{PHO5}-SrfIcs leu2::P_{lexO_4}-SrfI-T_{CYC1}-P_{ACT1}-LexA-ER-B112-T_{CYC1}-LEU2MX exo1::kanMX rad51::URA3MX	This paper	N/A

REAGENT or RESOURCE	**SOURCE**	**IDENTIFIER**
Saccharomyces cerevisiae W303: LSY5038-9C: *MAT*a *hocs::SrfIcs RAD5 hml::pRS-1 hmr::pRS-2 fpr1Δ RPL13A-2xFKBP12::TRP1 tor1-1 sgs1-frb-hphMX dna2-frb-hphMX met15Δ pho4::altNatMX P*$_{PHO5}$*-SrfIcs leu2::P*$_{lexO\_4}$*-SrfI-T*$_{CYC1}$*-P*$_{ACT1}$*-LexA-ER-B112-T*$_{CYC1}$*-LEU2MX exo1::kanMX rad51::URA3MX*	This paper	N/A
Saccharomyces cerevisiae W303: LSY5495-6B: *MAT*a *RAD5 hml::pRS-1 hmr::pRS-2 fpr1Δ RPL13A-2xFKBP12::TRP1 tor1-1 sgs1-frb-hphMX dna2-frb-hphMX met15Δ leu2::P*$_{lexO\_4}$*-HO-T*$_{CYC1}$*-P*$_{ACT1}$*-LexA-ER-B112-T*$_{CYC1}$*-LEU2MX exo1::kanMX chd1::natMX*	This paper	N/A
Saccharomyces cerevisiae W303: LSY5495-30D: *MAT*a *RAD5 hml::pRS-1 hmr::pRS-2 fpr1Δ RPL13A-2xFKBP12::TRP1 tor1-1 sgs1-frb-hphMX dna2-frb-hphMX met15Δ leu2::P*$_{lexO\_4}$*-HO-T*$_{CYC1}$*-P*$_{ACT1}$*-LexA-ER-B112-T*$_{CYC1}$*-LEU2MX exo1::kanMX*	This paper	N/A
Saccharomyces cerevisiae W303: LSY5496-2C: *MAT*a *RAD5 hml::pRS-1 hmr::pRS-2 fpr1Δ RPL13A-2xFKBP12::TRP1 tor1-1 sgs1-frb-hphMX dna2-frb-hphMX met15Δ leu2::P*$_{lexO\_4}$*-HO-T*$_{CYC1}$*-P*$_{ACT1}$*-LexA-ER-B112-T*$_{CYC1}$*-LEU2MX exo1::kanMX rsc2::natMX*	This paper	N/A
Saccharomyces cerevisiae W303: LSY5501-8D: *MAT*a *RAD5 hml::pRS-1 hmr::pRS-2 fpr1Δ RPL13A-2xFKBP12::TRP1 tor1-1 sgs1-frb-hphMX dna2-frb-hphMX met15Δ leu2::P*$_{lexO\_4}$*-HO-T*$_{CYC1}$*-P*$_{ACT1}$*-LexA-ER-B112-T*$_{CYC1}$*-LEU2MX exo1::kanMX snf5::kanMX*	This paper	N/A
Oligonucleotides		
Oligos for *in vitro* assays	Eurogentec	See Table S1
Primers for qPCR	Sigma	See Table S2
Adapters and primers for deep-sequencing library preparation	Integrated DNA Technologies; Sigma	See Table S3
Recombinant DNA		
Plasmid: pCAS	Ryan et al., 2014	Addgene Plasmid # 60847
Plasmid: pRG621: pFA6a-*FRB-T*$_{CYC2}$*-hphMX*	This paper	N/A
Plasmid: pRG638: pCAS with ZraI-XbaI for oligo-based sgRNA cloning	This paper	N/A
Plasmid: pRG646: pRG205MX-*P*$_{lexO\_4}$*-HO-T*$_{CYC1}$*-P*$_{ACT1}$*-LexA-ER-B112-T*$_{CYC1}$	Gnügge and Symington, 2020	Addgene Plasmid # 154815
Plasmid: pRG660: pRG205MX-*P*$_{lexO\_4}$*-SrfI-T*$_{CYC1}$*-P*$_{ACT1}$*-LexA-ER-B112-T*$_{CYC1}$	Gnügge and Symington, 2020	N/A
Plasmid: pRG662: pCAS with sgRNA targeting *bla*	This paper	N/A
Plasmid: pRG663: pCAS with sgRNA targeting chrIII:296712	This paper	N/A
Plasmid: pRG685: *P*$_{GAL1}$*-Citrine-T*$_{CYC1}$	This paper	N/A
Plasmid: pRG695: pCAS with sgRNA targeting *nat*	This paper	N/A
Plasmid: pRG696: pCAS with sgRNA targeting *MET15* (chrXII:733,324)	This paper	N/A
Plasmid: pRG704: pFA6a-*S. kudriavzevii P*$_{TEF1}$*-natMX-C. glabrata T*$_{TEF1}$	This paper	N/A
Plasmid: pRG712: pRG203MX- *P*$_{lexO\_4}$*-SrfI-T*$_{CYC1}$*-P*$_{ACT1}$*-LexA-ER-B112-T*$_{CYC1}$	Gnügge and Symington, 2020	N/A
Plasmid: pRG721: pRG203MX-*Citrine-HOcs-HA-T*$_{CYC1}$	This paper	N/A
Plasmid: pRG722: pRG201-*P*$_{ACT1}$*-mKate2-T*$_{CYC2}$*-HOcs*	This paper	N/A
Plasmid: pRG723: pRG201-*P*$_{TDH3}$*-mKate2-T*$_{CYC2}$*-HOcs*	This paper	N/A

REAGENT or RESOURCE	**SOURCE**	**IDENTIFIER**
Plasmid: pRG726: pBluescript-*hmr::*P_{GAL1}*-Citrine-*T_{CYC1}*-Ty1δ::hisG-HOcs*@chr3:295,659 repair template	This paper	N/A
Plasmid: pRG727: pBluescript-*hmr::(hmr-e::hisG-*P_{GAL1}*-Citrine-*T_{CYC1}*-hmr-i::hisG-Ty1δ::hisG-HOcs*@chr3:295,659) repair template	This paper	N/A
Plasmid: pRG738: pRG201-*mKate2-*T_{CYC2}*-HOcs*	This paper	N/A
Plasmid: pRG745: pRG203MX-P_{ACT1}*-Citrine-hisG-HOcs-HA-*T_{CYC1}	This paper	N/A
Plasmid: pRG746: pRG203MX-P_{TDH3}*-Citrine-hisG-HOcs-HA-*T_{CYC1}	This paper	N/A
Plasmid: pRG747: pBluescript-*pho4-SA1234PA6*	This paper	N/A
Plasmid: pRG759: pCAS with sgRNA targeting P_{PHO5} (chrII:431,486)	This paper	N/A
Plasmid: pRG778: pRG201-P_{TDH3}*-OsTIR1*	This paper	N/A
Plasmid: pTP391: expressing His-tagged yeast Mre11	Bhaskara et al., 2007	N/A
Plasmid: pFB-Xrs2-3xFLAG: expressing 3XFLAG-tagged yeast Xrs2	This paper	N/A
Plasmid: pFB-Rad50: expressing untagged yeast Rad50	Cannavo et al., 2013	N/A
Plasmid: pFB-MBP-Sae2-His: expressing MBP and His-tagged yeast Sae2	Cannavo et al., 2014	N/A
Plasmid: pFB-MBP-YKU70-his: expressing MBP and His-tagged yeast Ku70	Reginato et al., 2017	N/A
Plasmid: pFB-YKU80-FLAG: expressing FLAG-tagged yeast Ku80	Reginato et al., 2017	N/A
Plasmid: pAttP-S: vector for plasmid-length substrate	Cannavo et al., 2014	N/A
Software and algorithms		
bcl2fastq 2.20.0.422	Illumina	https://support.illumina.com/sequencing/sequencing_software/bcl2fastq-conversion-software/downloads.html
fastp 0.20.1	Chen et al., 2018	https://github.com/OpenGene/fastp
SAMtools 1.9	Li et al., 2009	http://www.htslib.org/download/
Bowtie 2.3.5.1	Langmead and Salzberg, 2012	http://bowtie-bio.sourceforge.net/bowtie2/index.shtml
UMI-tools 1.0.0	Smith et al., 2017	https://github.com/CGATOxford/UMI-tools
R 4.2.1	R Core Team, 2022	https://www.r-project.org/
GenomicRanges 1.48.0	Lawrence et al., 2013	https://bioconductor.org/packages/release/bioc/html/GenomicRanges.html
GenomicAlignments 1.32.0	Lawrence et al., 2013	https://bioconductor.org/packages/release/bioc/html/GenomicAlignments.html
BSgenome 1.64.0	Pagès, 2022	https://bioconductor.org/packages/release/bioc/html/BSgenome.html
Biostrings 2.64.0	Pagès et al., 2022	https://bioconductor.org/packages/release/bioc/html/Biostrings.html
Rmelting 1.12.0	Aravind and Krishna, 2022	https://www.bioconductor.org/packages/release/bioc/html/rmelting.html

REAGENT or RESOURCE	SOURCE	IDENTIFIER
Gviz 1.40.1	Hahne and Ivanek, 2016	https://bioconductor.org/packages/release/bioc/html/Gviz.html
ImageJ 1.53c	Schneider et al., 2012	https://imagej.nih.gov/ij/
Other		
microTUBEs	Covaris	Cat# 520045
SpeedBeads magnetic carboxylate modified particles	GE Healthcare	Cat# 65152105050250
Dynabeads M-280 Streptavidin	Invitrogen	Cat# 11205D
Zirconia/Silica Beads 0.5 mm	BioSpec	Cat# 11079105z
Micro Bio-Spin P-30 Gel Columns	Biorad	Cat# 7326223
Ni-NTA Agarose Resin	Qiagen	Cat# 30210
ANTI-FLAG® M2 Affinity Gel	Sigma	Cat# A2220
Amylose Resin	New England BioLabs	Cat# E8021L
Whatman® cellulose chromatography papers, 3MM Chr	Sigma	Cat# WHA3030917
RNA-seq data for G2-arrested *Saccharomyces cerevisiae* W303	Maya-Miles et al., 2019	GEO: GSE125258
S1-seq data for meiotic *Saccharomyces cerevisiae* SK1	Mimitou et al., 2017	SRA: PRJNA337955
resection-seq data for asynchronous *Saccharomyces cerevisiae* BY4741	Bazzano et al., 2021	SRA: PRJNA703820
LIFE SCIENCE TABLE WITH EXAMPLES FOR AUTHOR REFERENCE		
REAGENT or RESOURCE	**SOURCE**	**IDENTIFIER**
Antibodies		
Rabbit monoclonal anti-Snail	Cell Signaling Technology	Cat#3879S; RRID: AB_2255011
Mouse monoclonal anti-Tubulin (clone DM1A)	Sigma-Aldrich	Cat#T9026; RRID: AB_477593
Rabbit polyclonal anti-BMAL1	This paper	N/A
Bacterial and virus strains		
pAAV-hSyn-DIO-hM3D(Gq)-mCherry	Krashes et al., 2011	Addgene AAV5; 44361-AAV5
AAV5-EF1a-DIO-hChR2(H134R)-EYFP	Hope Center Viral Vectors Core	N/A
Cowpox virus Brighton Red	BEI Resources	NR-88
Zika-SMGC-1, GENBANK: KX266255	Isolated from patient (Wang et al., 2016)	N/A
Staphylococcus aureus	ATCC	ATCC 29213
Streptococcus pyogenes: M1 serotype strain: strain SF370; M1 GAS	ATCC	ATCC 700294
Biological samples		
Healthy adult BA9 brain tissue	University of Maryland Brain & Tissue Bank; http://medschool.umaryland.edu/btbank/	Cat#UMB1455
Human hippocampal brain blocks	New York Brain Bank	http://nybb.hs.columbia.edu/

REAGENT or RESOURCE	SOURCE	IDENTIFIER
Patient-derived xenografts (PDX)	Children’s Oncology Group Cell Culture and Xenograft Repository	http://cogcell.org/
Chemicals, peptides, and recombinant proteins		
MK-2206 AKT inhibitor	Selleck Chemicals	S1078; CAS: 1032350-13-2
SB-505124	Sigma-Aldrich	S4696; CAS: 694433-59-5 (free base)
Picrotoxin	Sigma-Aldrich	P1675; CAS: 124-87-8
Human TGF-β	R&D	240-B; GenPept: P01137
Activated S6K1	Millipore	Cat#14-486
GST-BMAL1	Novus	Cat#H00000406-P01
Critical commercial assays		
EasyTag EXPRESS 35S Protein Labeling Kit	PerkinElmer	NEG772014MC
CaspaseGlo 3/7	Promega	G8090
TruSeq ChIP Sample Prep Kit	Illumina	IP-202-1012
Deposited data		
Raw and analyzed data	This paper	GEO: GSE63473
B-RAF RBD (apo) structure	This paper	PDB: 5J17
Human reference genome NCBI build 37, GRCh37	Genome Reference Consortium	http://www.ncbi.nlm.nih.gov/projects/genome/assembly/grc/human/
Nanog STILT inference	This paper; Mendeley Data	http://dx.doi.org/10.17632/wx6s4mj7s8.2
Affinity-based mass spectrometry performed with 57 genes	This paper; Mendeley Data	Table S8; http://dx.doi.org/10.17632/5hvpvspw82.1
Experimental models: Cell lines		
Hamster: CHO cells	ATCC	CRL-11268
D. melanogaster: Cell line S2: S2-DRSC	Laboratory of Norbert Perrimon	FlyBase: FBtc0000181
Human: Passage 40 H9 ES cells	MSKCC stem cell core facility	N/A
Human: HUES 8 hESC line (NIH approval number NIHhESC-09-0021)	HSCI iPS Core	hES Cell Line: HUES-8
Experimental models: Organisms/strains		
C. elegans: Strain BC4011: srl-1(s2500) II; dpy-18(e364) III; unc-46(e177)rol-3(s1040) V.	Caenorhabditis Genetics Center	WB Strain: BC4011; WormBase: WBVar00241916
D. melanogaster: RNAi of Sxl: y[1] sc[*] v[1]; P{TRiP.HMS00609}attP2	Bloomington Drosophila Stock Center	BDSC:34393; FlyBase: FBtp0064874
S. cerevisiae: Strain background: W303	ATCC	ATTC: 208353
Mouse: R6/2: B6CBA-Tg(HDexon1)62Gpb/3J	The Jackson Laboratory	JAX: 006494
Mouse: OXTRfl/fl: B6.129(SJL)-Oxtr$^{tml.1Wsy}$/J	The Jackson Laboratory	RRID: IMSR_JAX:008471
Zebrafish: Tg(Shha:GFP)t10: t10Tg	Neumann and Nuesslein-Volhard, 2000	ZFIN: ZDB-GENO-060207-1

REAGENT or RESOURCE	**SOURCE**	**IDENTIFIER**
Arabidopsis: 35S::PIF4-YFP, BZR1-CFP	Wang et al., 2012	N/A
Arabidopsis: JYB1021.2: pS24(AT5G58010)::cS24:GFP(-G):NOS #1	NASC	NASC ID: N70450
Oligonucleotides		
siRNA targeting sequence: PIP5K I alpha #1: ACACAGUACUCAGUUGAUA	This paper	N/A
Primers for XX, see Table SX	This paper	N/A
Primer: GFP/YFP/CFP Forward: GCACGACTTCTTCAAGTCCGCCATGCC	This paper	N/A
Morpholino: MO-pax2a GGTCTGCTTTGCAGTGAATATCCAT	Gene Tools	ZFIN: ZDB-MRPHLNO-061106-5
ACTB (hs01060665_g1)	Life Technologies	Cat#4331182
RNA sequence: hnRNPAl_ligand: UAGGGACUUAGGGUUCUCUCUAGGGACUUAG GGUUCUCUCUAGGGA	This paper	N/A
Recombinant DNA		
pLVX-Tight-Puro (TetOn)	Clonetech	Cat#632162
Plasmid: GFP-Nito	This paper	N/A
cDNA GH111110	Drosophila Genomics Resource Center	DGRC:5666; FlyBase:FBcl0130415
AAV2/1-hsyn-GCaMP6- WPRE	Chen et al., 2013	N/A
Mouse raptor: pLKO mouse shRNA 1 raptor	Thoreen et al., 2009	Addgene Plasmid #21339
Software and algorithms		
ImageJ	Schneider et al., 2012	https://imagej.nih.gov/ij/
Bowtie2	Langmead and Salzberg, 2012	http://bowtie-bio.sourceforge.net/bowtie2/index.shtml
Samtools	Li et al., 2009	http://samtools.sourceforge.net/
Weighted Maximal Information Component Analysis v0.9	Rau et al., 2013	https://github.com/ChristophRau/wMICA
ICS algorithm	This paper; Mendeley Data	http://dx.doi.org/10.17632/5hvpvspw82.1
Other		
Sequence data, analyses, and resources related to the ultra-deep sequencing of the AML31 tumor, relapse, and matched normal	This paper	http://aml31.genome.wustl.edu
Resource website for the AML31 publication	This paper	https://github.com/chrisamiller/aml31SuppSite
PHYSICAL SCIENCE TABLE WITH EXAMPLES FOR AUTHOR REFERENCE		
REAGENT or RESOURCE	**SOURCE**	**IDENTIFIER**
Chemicals, peptides, and recombinant proteins		
QD605 streptavidin conjugated quantum dot	Thermo Fisher Scientific	Cat#Q10101MP
Platinum black	Sigma-Aldrich	Cat#205915
Sodium formate BioUltra, ≥99.0% (NT)	Sigma-Aldrich	Cat#71359
Chloramphenicol	Sigma-Aldrich	Cat#C0378
Carbon dioxide (^{13}C, 99%) (<2% ^{18}O)	Cambridge Isotope Laboratories	CLM-185-5

REAGENT or RESOURCE	**SOURCE**	**IDENTIFIER**
Poly(vinylidene fluoride-co-hexafluoropropylene)	Sigma-Aldrich	427179
PTFE Hydrophilic Membrane Filters, 0.22 μm, 90 mm	Scientificfilters.com/TischScientific	SF13842
Critical commercial assays		
Folic Acid (FA) ELISA kit	Alpha Diagnostic International	Cat# 0365-0B9
TMT10plex Isobaric Label Reagent Set	Thermo Fisher	A37725
Surface Plasmon Resonance CM5 kit	GE Healthcare	Cat#29104988
NanoBRET Target Engagement K-5 kit	Promega	Cat#N2500
Deposited data		
B-RAF RBD (apo) structure	This paper	PDB: 5J17
Structure of compound 5	This paper; Cambridge Crystallographic Data Center	CCDC: 2016466
Code for constraints-based modeling and analysis of autotrophic *E. coli*	This paper	https://gitlab.com/elad.noor/sloppy/tree/master/rubisco
Software and algorithms		
Gaussian09	Frish et al., 2013	https://gaussian.com
Python version 2.7	Python Software Foundation	https://www.python.org
ChemDraw Professional 18.0	PerkinElmer	https://www.perkinelmer.com/category/chemdraw
Weighted Maximal Information Component Analysis v0.9	Rau et al., 2013	https://github.com/ChristophRau/wMICA
Other		
DASGIP MX4/4 Gas Mixing Module for 4 Vessels with a Mass Flow Controller	Eppendorf	Cat#76DGMX44
Agilent 1200 series HPLC	Agilent Technologies	https://www.agilent.com/en/products/liquid-chromatography
PHI Quantera II XPS	ULVAC-PHI, Inc.	https://www.ulvac-phi.com/en/products/xps/phi-quantera-ii/